Journal of Computational Physics 359 (2018) 106–136

Contents lists available at ScienceDirect

Journal of Computational Physics

www.elsevier.com/locate/jcp

Multi-resolution MPS method

Masayuki Tanaka [a,b,*], Rui Cardoso [a], Hamid Bahai [a]

[a] Brunel University London, Kingston Lane, Uxbridge, London, UB8 3PH, United Kingdom
[b] Corporate Manufacturing Engineering Center, Toshiba Co., Ltd., 33, Shinisogo-cho, Isogo-ku, Yokohama-shi, Kanagawa, 235-0017, Japan

ARTICLE INFO

Article history:
Received 27 July 2017
Received in revised form 27 November 2017
Accepted 29 December 2017
Available online 12 January 2018

Keywords:
Particle method
Least square MPS method
Multi-resolution
Incompressible fluid
Wall boundary
Pressure boundary

ABSTRACT

In this work, the Moving Particle Semi-implicit (MPS) method is enhanced for multi-resolution problems with different resolutions at different parts of the domain utilising a particle splitting algorithm for the finer resolution and a particle merging algorithm for the coarser resolution. The Least Square MPS (LSMPS) method is used for higher stability and accuracy. Novel boundary conditions are developed for the treatment of wall and pressure boundaries for the Multi-Resolution LSMPS method. A wall is represented by polygons for effective simulations of fluid flows with complex wall geometries and the pressure boundary condition allows arbitrary inflow and outflow, making the method easier to be used in flow simulations of channel flows. By conducting simulations of channel flows and free surface flows, the accuracy of the proposed method was verified.

1. Introduction

Full-Lagrangian particle methods have great advantages when compared with Eulerian methods due to the fact that the particle can move dynamically and there is no need to calculate the advection terms as in Eulerian methods. The absence of the advection terms makes it easier to simulate a free surface flow, that has been one of the most beneficial advantages of particle methods. Also, because connections to adjacent particles can be updated easily, the well-known excessive distortion problems common of a Lagrangian finite element procedure can be avoided. Originally, the Smoothed Particle Hydrodynamics (SPH) method, which is one of the most popular full-Lagrangian methods, was developed to simulate compressible fluid flows [32,7]. This method has been widely used to simulate not only compressible fluid but also incompressible fluid assuming that the fluid is weakly compressible. On the other hand, the Moving Particle Semi-implicit (MPS) method was developed to simulate incompressible fluid flow strictly within a full-Lagrangian context [23–25]. Although the basic concept of the MPS method is similar to the SPH method, the MPS method is unique because of the pressure term in the Navier–Stokes equation that is calculated implicitly by imposing the incompressible condition. A similar technique has been applied to SPH method and it is called the Incompressible SPH (ISPH) method [3].

The MPS method has been widely used to simulate incompressible fluid flows for several different applications such as the mixing of fluid as in the work of Matsunaga et al. [35], the numerical simulation of sloshing with large deforming free surfaces, Pan et al. [43], the three-dimensional numerical analysis of shipping water onto a moving ship, Shibata et al. [46], the numerical analysis of tsunami–structure interactions, Huang and Zhu [13], the numerical prediction of oil amount leaked from a damaged tank, Jeong et al. [15], the 3D simulation of the melting of metallic alloys, Mustari et al. [39], the numerical

* Corresponding author.
E-mail address: masayuki11.tanaka@toshiba.co.jp (M. Tanaka).

https://doi.org/10.1016/j.jcp.2017.12.042

analysis of two-dimensional welding process, Saso et al. [45], the solidification of aluminium alloys in semi-solid forging processes, Regmi et al. [44], the simulation of Human swallowing, Kikuchi et al. [20] and the simulation of haemodynamics of small vessels, Gambaruto et al. [6].

However, the MPS method has a key fundamental instability problem that can deteriorate the accuracy of the solution considerably and even lead to a total failure of the simulation. It is well known that particle behaviour becomes unstable when attracting forces act between particles and this is called as tensile instability [51]. This problem is also very common in the SPH methods and there has been already many good research to handle tensile instability: Monaghan [37] introduced the artificial pressure technique to tackle tensile instability, Swegle et al. [51] explained the tensile instability by stating that it occurs when the direction of the force and the gradient of the kernel function were not consistent, Yang et al. [62] proposed a new kernel function whose second derivative was always positive and they showed that the tensile instability disappeared when this kernel function was used. However, Yang's kernel function cannot be applied to the MPS method because the second derivative of the kernel function does not appear in the MPS method.

The major cause for the source of tensile instability in the MPS method is the negative pressure around free surfaces of the flow and two techniques are commonly used to avoid the instability: altering the pressure gradient term and neglecting the negative pressure. In the former technique, the pressure gradient is evaluated by removing attracting forces. In the latter, the negative pressure is modified artificially to zero. These are not strict formulations but they are useful to improve stability. Using these techniques, the MPS method achieves great stability, however, they has been still suffering from inaccuracy.

Another potential source of instability is due to the inconsistency of the formulation of the MPS method. The MPS method is usually formulated by assuming that particles are arranged/distributed uniformly. The source of instability starts to be more evident when consistency is lost due to the non-uniform arrangement of particles as the simulation goes on. This inconsistency also leads to the loss of accuracy. The incompressible condition of the MPS method, which enforces the particle number density to be constant, is also one of the major sources for the loss of accuracy on the MPS method.

Many research was conducted in the past to improve the stability and accuracy of the MPS method. Tanaka and Masunaga [55] proposed a new formulation of the source term in the Poisson equation for pressure. Kondo and Koshizuka [22] proposed another formulation of the source term and this method was improved by Khayyer and Gotoh [17]. Shibata et al. [48] introduced the virtual particles method for the treatment of the negative pressure instability. Khayyer and Gotoh [16] altered the Laplacian model in 2D analysis and further extended it for 3D domains [18]. There has been some other relevant research for the improvement of the Laplacian model [41,53]. Tamai and Koshizuka [52] have proposed the Least Square MPS (LSMPS) method to overcome the inaccuracies caused by the non-uniform particle distribution and other similar methods were proposed for the SPH method [4,5].

Another limitation of the fully-Lagrangian particles method is computational cost. Generally, a particle method requires more computational resources when compared with an Eulerian method because of the extra computational effort required to handle particle interactions. However, some research was already conducted to tackle or minimise this issue by using multi-threading with multi-core CPU or GPU [11,65,38].

In Eulerian methods, changing the resolution of the discretisation for different parts of the domain is one of most distinguished characteristics of the method to reduce computational cost. In a Lagrangian description, the resolution, i.e. diameters of particles, is generally limited and non-uniform size diameters cannot be used. There were several attempts to change the spatial resolution in the SPH methods: Kitsionas and Whitworth [21] proposed the particle splitting method to increase the spatial resolution locally. In this method a particle is split into thirteen particles to obtain a spherically symmetric kernel function; Lastiwka et al. [27] proposed changing resolution by adding or removing particles. They applied a first-order differentiation scheme and showed that it was accurate even if particles had non-uniform spacing; Liu et al. [31] proposed the Adaptive SPH (ASPH) method, in which a support domain was extended to non-spherical regions such as an ellipsoidal shape region for example; Adams et al. [2] proposed a method to change the spatial resolution adaptively. All of the multi-resolution techniques developed for the SPH methods are based on formulations for a compressible fluid flow, therefore changing resolution is comparatively easy in this case.

A multi-resolution simulation for the MPS method is more difficult to be achieved because of the pressure term that has to be solved implicitly. However, there were some noteworthy developments for multi-resolution techniques for the MPS method such as the works of Shibata et al. [47] on the overlapping technique and Tang et al. [56] for the extension of Shibata's work to three dimensions. Notwithstanding the great contributions of Shibata and Tang for multi-resolution methods for the MPS method, there is still a major drawback which is the inability of the technique to allow for two-way interactions between low-resolution and high-resolution domains. Tanaka et al. [54] developed further a multi-resolution technique for the MPS method in two dimensions, however, the formulation was derived for the classical MPS method and thus it suffers from inaccuracy and stability issues. Tang et al. [57] extended this method for three dimensions, however, no splitting or merging algorithms were adopted and therefore the spatial resolution cannot be changed dynamically. The major conclusion to be taken is that a high accuracy and stability multi-resolution particle method for incompressible fluid flow still needs to be developed.

In this paper, the Multi-Resolution MPS method, which can change spatial resolution dynamically in incompressible fluid flow simulations is presented. New boundary conditions such as a wall and a pressure boundary conditions for multi-resolution simulations are also proposed.

2. Preliminary

2.1. Nomenclature

The commonly used symbols are referred below.

$\boldsymbol{x}$	Position
$\boldsymbol{u}$	Velocity
$\boldsymbol{n}$	Normal vector
$\boldsymbol{f}$	Acceleration of the gravity
t	Time
Δt	Size of the time step
d	Number of dimensions
ρ	Density
ν	Kinematic viscosity
P	Pressure
r	Distance
R	Effective radius
L	Diameter of particles
w	Weight function
n	Particle number density
n^*	Criterion of the particle number density

User defined parameters and recommended/default values to be used in the simulations are listed below.

α_d	0.97	Threshold to detect surface particles
α_c	0.3	Threshold to detect isolated particles
α_θ	2.1	Effect radius ratio for surface detection
α_P	0.05–0.20	Relaxation coefficient for the source term
c_{max}	1.2	Upper tolerance of the packing ratio for the incompressible state
c_{min}	0.95	Lower tolerance of the packing ratio for the incompressible state
c'_{max}	1.001	Upper limit for volume change
c'_{min}	0.999	Lower limit for volume change
α_C	0.1	Relaxation coefficient for the Courant condition
α_e	0.6	Threshold of error function in particle splitting
α_t	0.7	Distance ratio in particle splitting
α_r	1.5	Distance ratio in particle merging
α_w	1.0	Distance ratio in wall boundary
α_o	0.25	Distance ratio of outflow in pressure boundary
α_i	0.25	Distance ratio of inflow in pressure boundary
α_I	1.0	Distance ratio of inflow judgement
α_s	2.5e–4	Distance ratio in particle shifting
α_g	0.001	Threshold for distance in particle shifting
α_T	0.8	Threshold for target distance in particle shifting
α_p	0.1	Penalty tolerance ratio in particle shifting
α_S	0.01	Distance ratio for upper limit in particle shifting

2.2. Notation

An arbitrary relative scalar and vector between particle i and j are defined as:

$$\phi_{ij} = \phi_j - \phi_i \tag{1}$$

for the relative scalar and:

$$\boldsymbol{\Phi}_{ij} = \boldsymbol{\Phi}_j - \boldsymbol{\Phi}_i \tag{2}$$

for the relative vector form. The exception to this notation is the definition of the distance between particle i and j which in this case will be denoted by:

$$r_{ij} = \left|\boldsymbol{x}_j - \boldsymbol{x}_i\right|. \tag{3}$$

The notation that is going to be used for the definition of a generic variable ϕ at a time step k is going to be ϕ^k. This rule is also going to be applied to the derivative operator ∇ in the form described by the following equation:

$$\nabla^k \phi = \frac{\partial \phi}{\partial \boldsymbol{x}^k} \tag{4}$$

Variables defined for a boundary Γ are going to be represented as $\phi|_\Gamma$. This rule is also going to be applied to formulations defined for a boundary as $\phi = \phi'|_\Gamma$.

A fluid particle i is denoted by $i \in \mathcal{F}$, a wall particle by $i \in \mathcal{W}$ and a pressure boundary particle by $i \in \mathcal{P}$.

2.3. Governing equations

In this paper, the models, methods and algorithms developed were designed for the analysis of incompressible fluid flow where the major governing equation is the Navier–Stokes equation which is comprised of the pressure term, the viscosity term and the external force term:

$$\frac{D\boldsymbol{u}}{Dt} = -\frac{1}{\rho}\nabla P + \nu \nabla^2 \boldsymbol{u} + \boldsymbol{f} \tag{5}$$

The incompressible condition is enforced through the use of the continuity equation for incompressible fluids:

$$\nabla \cdot \boldsymbol{u} = 0 \tag{6}$$

3. Traditional MPS method

3.1. Derivative models

In the traditional MPS method, particle interactions are evaluated using a weight function w, which is a function of the distance r between particles and the effective radius R of the support domain:

$$w(r, R) = \begin{cases} \dfrac{R}{r} - 1 & (r \le R) \\ 0 & (r > R) \end{cases} \tag{7}$$

The sum of the weight functions in the support domain is commonly known as the particle number density n_i and it is defined as:

$$n_i = \sum_{j \neq i} w_{ij}, \tag{8}$$

where $w_{ij} = w\left(r_{ij}, R\right)$ is the weight function between particle i and j. The particle number density when particles are located on a regular grid whose grid size is the same with the diameter of the particles is called the criterion of particle number density n^*.

In the derivative models for the traditional MPS method, the differential operators for the gradient, the Laplacian and the divergence of a particle i are formulated as follows:

$$\langle \nabla \phi \rangle_i = \frac{d}{n^*} \sum_{j \neq i} \frac{\phi_{ij}}{r_{ij}^2} \boldsymbol{x}_{ij} w_{ij}, \tag{9}$$

$$\left\langle \nabla^2 \phi \right\rangle_i = \frac{2d}{n^* \lambda_i} \sum_{j \neq i} \phi_{ij} w_{ij}, \tag{10}$$

$$\langle \nabla \cdot \boldsymbol{\Phi} \rangle_i = \frac{d}{n^*} \sum_{j \neq i} \frac{\boldsymbol{\Phi}_{ij} \cdot \boldsymbol{x}_{ij}}{r_{ij}^2} w_{ij}, \tag{11}$$

where ϕ is an arbitrary scalar, $\boldsymbol{\Phi}$ is an arbitrary vector and λ is a coefficient in the Laplacian model which is defined as:

$$\lambda_i = \frac{\sum_{j \neq i} w_{ij} r_{ij}^2}{\sum_{j \neq i} w_{ij}}. \tag{12}$$

Note that it is widely known that these differential operator models are formulated assuming that particles are arranged uniformly and they tend to lose their accuracy with a non-uniform particle arrangement [52].

3.2. Time integration

The typical procedure to solve the Navier–Stokes equation is as follows. All terms, with the exception of the pressure term, are firstly computed through the following explicit time integration scheme:

$$\frac{\boldsymbol{u}^{k'} - \boldsymbol{u}^k}{\Delta t} = \nu \nabla^2 \boldsymbol{u}^k + \boldsymbol{f}, \tag{13}$$

where $\boldsymbol{u}^{k'}$ is a temporary velocity vector which is obtained after resolving explicit terms. Secondly, the positions are updated temporarily to evaluate the particle number density after calculating the explicit term.

$$\boldsymbol{x}^{k'} = \boldsymbol{x}^k + \Delta t \boldsymbol{u}^{k'}. \tag{14}$$

Thirdly, the pressure term is resolved implicitly by taking into consideration the fluid incompressible condition from the use of the continuity equation as follows:

$$\frac{\boldsymbol{u}^{k+1} - \boldsymbol{u}^{k'}}{\Delta t} = -\frac{1}{\rho} \nabla P^{k+1} \tag{15}$$

After velocities are calculated, positions are updated using the Euler implicit scheme:

$$\boldsymbol{x}^{k+1} = \boldsymbol{x}^k + \Delta t \boldsymbol{u}^{k+1}. \tag{16}$$

3.3. Imposing the incompressible conditions

Two kinds of incompressible conditions have been suggested in the MPS method. The first incompressible condition used is based on the idea that the particle number density is kept constant if the fluid is incompressible, i.e.:

$$n_i^{k+1} = n^*. \tag{17}$$

Using this condition the following Poisson's equation is derived and the pressure is evaluated by solving this equation.

$$\frac{1}{\rho} \nabla^2 P^{k+1} = \frac{1}{\Delta t^2} \frac{n^* - n^{k'}}{n^*} \tag{18}$$

where $n^{k'}$ is a temporary particle number density obtained after computation of the explicit terms from Eq. (13). In this work, this incompressible condition is referred as the Particle Number Density (PND) condition.

The second incompressible condition that can be used is based on the zero divergence of the velocity field. By applying the divergence at both members of Eq. (15) and by using the incompressible condition from Eq. (6), the following Poisson's equation can be derived:

$$\frac{1}{\rho} \nabla^2 P^{k+1} = \frac{1}{\Delta t} \nabla \cdot \boldsymbol{u}^{k'} \tag{19}$$

This equation is also used in the Meshless Advection using Flow-directional Local-grid (MPS-MAFL) method [63,26,10] in which the particle distribution is not uniform. When this incompressible condition is applied, the temporary position update expressed by Eq. (14) is not needed. This second incompressible condition from Eq. (19) is referred as the Divergence Free (DF) condition in this paper.

For the calculation of the Poisson's equation of the pressure, the Dirichlet boundary condition for free surface particles is required, i.e. a constant value (normally, zero) is set to the pressure of the free surface particles. Surface particles are likely to have a reduced number of particles in their support domain when compared with interior particles. Particles with particle number density lower than a specific threshold α_d of the initial particle number density n^0 are considered to be surface particles, i.e.:

$$n_i < \alpha_d n^*. \tag{20}$$

In addition, the Neumann boundary condition for wall particles are also required to solve the Poisson's equation normally, however, wall particles are treated as well as fluid particles in the pressure calculation and the boundary condition of wall particles is not referred in the traditional MPS method.

Once the pressure is calculated, the velocity correction is evaluated by the gradient of the pressure from Eq. (15). To apply the gradient model of the MPS method to Eq. (15), the velocity variation in the pressure term is represented as

$$\frac{\boldsymbol{u}^{k+1} - \boldsymbol{u}^{k'}}{\Delta t} = -\frac{1}{\rho} \frac{d}{n^*} \sum_{j \neq i} \frac{P_j - P_i}{r_{ij}^2} \boldsymbol{x}_{ij} w_{ij}. \tag{21}$$

However, it is commonly known that this equation might lead to tensile instability. Therefore, the following equation is used instead for stabilisation.

$$\frac{\boldsymbol{u}^{k+1}-\boldsymbol{u}^{k'}}{\Delta t}=-\frac{1}{\rho}\frac{d}{n^*}\sum_{j\neq i}\frac{P_j-\hat{P}_i}{r_{ij}^2}\boldsymbol{x}_{ij}w_{ij}, \tag{22}$$

where $\hat{P}_i$ is the minimum pressure among neighbouring particles within the support domain of particle i. Using this formulation, all particle interaction forces become repulsive and the simulation becomes more stable.

3.4. Limitations and recent developments

Although the MPS method is for simulating incompressible fluid flow, some techniques are needed to obtain plausible particle behaviours. For example, solving the Eq. (18) leads to particle explosion due to high pressure. A common practice is to affect the source term with a relaxation coefficient α_P so that a smaller source term can be obtained [48]:

$$\frac{1}{\rho}\nabla^2 P^{k+1}=\frac{\alpha_P}{\Delta t^2}\frac{n^*-n^{k'}}{n^*} \tag{23}$$

Another way to prevent particle explosion is to consider restricted compressibility, as in the work of Ikeda et al. [14]. In this case, the Poisson's equation of pressure is re-written as follows:

$$\frac{1}{\rho}\nabla^2 P^{k+1}=\frac{1}{\Delta t^2}\left(\frac{n^*-n^{k'}}{n^*}+\frac{P^{k+1}}{s^2}\right), \tag{24}$$

where s is the speed of sound. Considering restricted compressibility, the simulation becomes more stable [14].

Tanaka and Masunaga [55] pointed out that the volume has not been conserved using the DF condition alone and proposed to combine the source terms from the PND and DF conditions as follows:

$$\frac{1}{\rho}\nabla^2 P^{k+1}=\frac{1}{\Delta t}\nabla\cdot\boldsymbol{u}^{k'}+\frac{\alpha_P}{\Delta t^2}\frac{n^*-n^{k'}}{n^*} \tag{25}$$

Using this Poisson's equation, smoother pressure distribution can be obtained and volume change can be prevented with an proper parameter α_P. This formulation for the Poisson's equation has been widely used, however, the relaxation coefficient α_P depends on the simulation conditions [29,50].

It is common practice to force the pressure value to zero if a negative pressure is obtained from the solution of the Poisson's equation to avoid the tensile instability. Shibata et al. [48] improved some formulations in the MPS method using virtual particles and demonstrated that the negative pressure was able to be treated without instability. The same concept was also proposed by Tsuruta et al. [59].

4. Multi-resolution MPS method

4.1. Defined parameters

Simulations with multi-resolution are more challenging due to the fact that particles have various diameters and some traditional techniques such as keeping the particle number density constant and detecting surface particles from the particle number density cannot be applied anymore. It is thus necessary to introduce here some important definitions for multi-resolution simulations for the MPS method.

The first definition to be introduced is the volume of a particle. The volume of each particle V_i is defined as the diameter L_i to the power of the number of dimensions d:

$$V_i=L_i^d \tag{26}$$

Each particle has its own effective radius which depends on its diameter as follows:

$$R_i=R_eL_i \tag{27}$$

where R_e is an effective radius ratio and $R_e=3.1$ is used in this paper. When particles have different diameters, interaction faults might occur in some situations. As shown in Fig. 1, a larger particle could lay outside of an effective radius of a smaller particle although the smaller particle is in the effective radius of the larger particle. This interaction fault might cause inaccuracy or instability and therefore the effective radius R between particle i and j is defined as an average of each effective radius.

$$R_{ij}=\frac{R_i+R_j}{2} \tag{28}$$

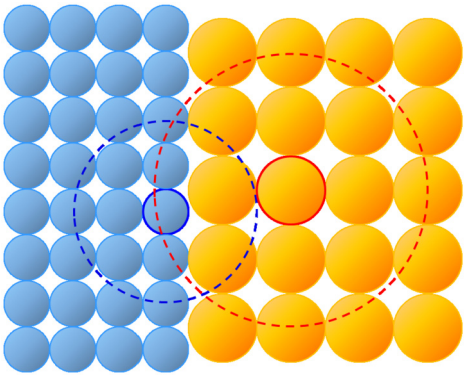

Fig. 1. Interaction fault in a multi-resolution particle arrangement.

By defining the effective radius R_{ij} like this, the interaction is always calculated on both particles even if the diameters differ. The weight function is then be calculated as below:

$$w_{ij} = w\left(r_{ij}, R_{ij}\right) = \begin{cases} \left(\dfrac{r_{ij}}{R_{ij}} - 1\right)^2 & \left(r_{ij} \le R_{ij}\right) \\ 0 & \left(r_{ij} > R_{ij}\right) \end{cases} \tag{29}$$

The Multi-Resolution MPS method requires the weight function to be defined or non-singular for pair of particles at zero distance between each other while the weight function from Eq. (7), which is frequently used in traditional MPS methods, is singular at zero distance. This weight function has been utilised in other works as well [22,52].

Every particle has a normal vector $\boldsymbol{n}_i$ which is particularly useful for the definition of boundary conditions. The normal vectors of fluid particles are calculated from the following set of equations:

$$\boldsymbol{n}_i = \frac{\boldsymbol{n}_i^*}{\left|\boldsymbol{n}_i^*\right|} \tag{30}$$

$$\boldsymbol{n}_i^* = \left[\sum_{j \neq i} w_{ij} \boldsymbol{x}_{ij} \otimes \boldsymbol{x}_{ij}\right]^{-1} \sum_{j \neq i} w_{ij} \boldsymbol{x}_{ij} \tag{31}$$

The normal vectors of wall particles are computed from wall geometries. Note that normal vectors of a fluid particle and a wall particle have directions toward outside of fluid and toward fluid respectively.

For the multi-resolution simulations the packing ratio c_i is used instead of the particle number density:

$$c_i = \frac{N_i}{V_R} \tag{32}$$

where V_R is the volume within the effective radius:

$$V_R\left(R\right) = \begin{cases} \pi R^2 & (2D) \\ \frac{4}{3}\pi R^3 & (3D) \end{cases} \tag{33}$$

and N_i is the particle volume within the effective radius R and it is defined by:

$$N_i\left(R\right) = \sum_{j \in \mathcal{F}} W_{ij}\left(R\right) + \sum_{j \in \mathcal{W}} W_{ij}^*\left(R\right), \tag{34}$$

where W is a volume function for fluid particles and W^* is for wall particles.

$$W_{ij}\left(R\right) = \begin{cases} 0.0 & \left(R < r_{ij} - \dfrac{L_j}{2}\right) \\ \dfrac{R - r_{ij} + \frac{L_j}{2}}{L_j} V_j & \left(r_{ij} - \dfrac{L_j}{2} \le R \le r_{ij} + \dfrac{L_j}{2}\right) \\ V_j & \left(r_{ij} + \dfrac{L_j}{2} < R\right) \end{cases} \tag{35}$$

$$W_{ij}^{*}(R) = \begin{cases} 0.0 & \left(R < r_{ij} - \dfrac{L_j}{2}\right) \\ \dfrac{R - r_{ij} + \frac{L_j}{2}}{L_j} V_j & \left(r_{ij} - \dfrac{L_j}{2} \le R\right) \end{cases} \tag{36}$$

The particle volume N_i depends on the effective radius and is likely to oscillate. So, the particle volume is calculated with multiple effective radii and is approximated by the least square method using the error function E as defined below:

$$E_i = \sum_{a=0}^{A-1} (c_i V_R - \langle N_i \rangle_a)^2 \tag{37}$$

$$\langle N_i \rangle_a = N_i (\langle R_i \rangle_a) \tag{38}$$

$$\langle R_i \rangle_a = \frac{L_i}{2} + \frac{a (R_i - L_I)}{A - 1} \quad (a = 0, 1, \cdots, A-1) \tag{39}$$

where A is the number of the effective radii used for the calculations. Then, the packing ratio for particle i is evaluated as follows:

$$c_i = \frac{\sum_{a=0}^{A-1} \langle N_i \rangle_a \langle R_i \rangle_a}{\sum_{a=0}^{A-1} \pi \langle R_i \rangle_a}. \tag{40}$$

By using this packing ratio the density around each particle can be calculated approximately and then the gradient of density can be calculated as well even if there exist various sizes of particles. Note that this packing ratio is just an approximation of the density and is not an accurate value. Therefore, careful consideration is necessary when this packing ratio is used for the enforcement of the incompressible condition although this works well for surface detection and for other algorithmic procedures required for particle flow simulations.

4.2. Least square formulation

A new formulation for the differential operators is needed for multi-resolution simulations because the traditional MPS method is formulated assuming that all the particles have the same diameter and a uniform arrangement. The LSMPS method [52], which recreates differential operators based on neighbouring particle positions for every time step, can provide more accurate approximation even if particles are arranged randomly. For this reason, the LSMPS method is specially suitable for multi-resolution simulations.

There are two kinds of LSMPS formulations: type A and type B. LSMPS type A is for calculating differential operators on a particle and LSMPS type B is for calculating differential operators at an arbitrary position. The formulation of LSMPS type A is shown next.

$$\boldsymbol{D}_{\boldsymbol{x}} f(\boldsymbol{x})|_{\boldsymbol{x}_i} = \boldsymbol{H}_i \left[\boldsymbol{M}_i^{-1} \boldsymbol{b}_i \right] \tag{41}$$

where $\boldsymbol{D}_{\boldsymbol{x}}$ is a differential operator, $\boldsymbol{H}$ is a matrix of coefficients, $\boldsymbol{M}$ is a moment matrix and $\boldsymbol{b}$ is a moment vector. The second order formulation for two dimensions, for example, is represented as below:

$$\boldsymbol{D}_{\boldsymbol{x}} = \left[\frac{\partial}{\partial x}, \frac{\partial}{\partial y}, \frac{\partial^2}{\partial^2 x}, \frac{\partial}{\partial x \partial y}, \frac{\partial^2}{\partial^2 y} \right]^T \tag{42}$$

$$\boldsymbol{H}_i = \begin{bmatrix} L_i^{-1} & 0 & 0 & 0 & 0 \\ 0 & L_i^{-1} & 0 & 0 & 0 \\ 0 & 0 & 2L_i^{-1} & 0 & 0 \\ 0 & 0 & 0 & L_i^{-1} & 0 \\ 0 & 0 & 0 & 0 & 2L_i^{-1} \end{bmatrix} \tag{43}$$

$$\boldsymbol{M}_i = \sum_{j \neq i} \left[w_{ij} \boldsymbol{p}\left(\frac{\boldsymbol{x}_{ij}}{L_i}\right) \otimes \boldsymbol{p}\left(\frac{\boldsymbol{x}_{ij}}{L_i}\right) \right] \tag{44}$$

$$\boldsymbol{b}_i = \sum_{j \neq i} \left[w_{ij} \boldsymbol{p}\left(\frac{\boldsymbol{x}_{ij}}{L_i}\right) f_{ij} \right] \tag{45}$$

$$\boldsymbol{p}(\boldsymbol{x}) = \left[x, y, x^2, xy, y^2\right]^T \tag{46}$$

By using this formulation, every derivative can then be calculated. Note that there are no individual models for the gradient, Laplacian and divergence operators like for the traditional MPS method, meaning that these operators have to be calculated by each derivative for the LSMPS method.

The formulation for the LSMPS type B is shown below.

$$\hat{\boldsymbol{D}}_{\boldsymbol{x}} f(\boldsymbol{x})\Big|_{\boldsymbol{x}} = \hat{\boldsymbol{H}}\left[\hat{\boldsymbol{M}}^{-1}\hat{\boldsymbol{b}}\right] \tag{47}$$

where $\hat{\boldsymbol{D}}_{\boldsymbol{x}}$ is a derivative operator, $\hat{\boldsymbol{H}}$ is a matrix of coefficients, $\hat{\boldsymbol{M}}$ is a moment matrix and $\hat{\boldsymbol{b}}$ is a moment vector. The second order formulation for 2 dimensions for example is represented as below.

$$\hat{\boldsymbol{D}}_{\boldsymbol{x}} = \left[1, \frac{\partial}{\partial x}, \frac{\partial}{\partial y}, \frac{\partial^2}{\partial^2 x}, \frac{\partial}{\partial x \partial y}, \frac{\partial^2}{\partial^2 y}\right]^T \tag{48}$$

$$\hat{\boldsymbol{H}} = \begin{bmatrix} 1 & 0 & 0 & 0 & 0 & 0 \\ 0 & l^{-1} & 0 & 0 & 0 & 0 \\ 0 & 0 & l^{-1} & 0 & 0 & 0 \\ 0 & 0 & 0 & 2l^{-1} & 0 & 0 \\ 0 & 0 & 0 & 0 & l^{-1} & 0 \\ 0 & 0 & 0 & 0 & 0 & 2l^{-1} \end{bmatrix} \tag{49}$$

$$\hat{\boldsymbol{M}} = \sum_i \left[w_i \hat{\boldsymbol{p}}\left(\frac{\boldsymbol{x}_i - \boldsymbol{x}}{l}\right) \otimes \hat{\boldsymbol{p}}\left(\frac{\boldsymbol{x}_i - \boldsymbol{x}}{l}\right)\right] \tag{50}$$

$$\hat{\boldsymbol{b}} = \sum_i \left[w_i \hat{\boldsymbol{p}}\left(\frac{\boldsymbol{x}_i - \boldsymbol{x}}{l}\right) f_i\right] \tag{51}$$

$$\hat{\boldsymbol{p}}(\boldsymbol{x}) = \left[1, x, y, x^2, xy, y^2\right]^T \tag{52}$$

l is an average diameter around the position $\boldsymbol{x}$. The LSMPS type B can calculate the derivative operator at any point, however, the operator has one more component than the LSMPS type A. Therefore if the derivative operator is calculated at a particle position, the LSMPS type A is normally utilised.

4.3. Incompressible condition

Theoretically, the incompressible condition is expressed by Eq. (6). However, there are two expressions for this equation to impose the incompressible condition at the time step k:

$$\nabla^k \cdot \boldsymbol{u} = 0, \tag{53}$$

$$\nabla^{k+1} \cdot \boldsymbol{u} = 0. \tag{54}$$

Normally, Eq. (53) is used because it is easier to be applied for the calculation of the pressure term. However, this expression would not lead to strict incompressible state because the divergence of the velocity field after updating positions is not zero. Furthermore, the volume would not be conserved and some techniques are then needed to keep the volume constant. This is why the combination of the two incompressible conditions, i.e. the PND condition and the DF condition, have been widely used [55]. For more strict incompressibility, Eq. (54) should be applied instead.

Nair and Tomar [40] adopted a different approach for volume conservation and proposed another incompressible condition as below:

$$\det \boldsymbol{F}^k = 1 \tag{55}$$

where $\boldsymbol{F}$ is the deformation gradient tensor defined as:

$$\boldsymbol{F}^k = \nabla^k \boldsymbol{x}^{k+1} \tag{56}$$

If the time integration scheme from Eq. (15) and Eq. (16) is used, the deformation gradient can be represented as a function of the pressure as follows:

$$\boldsymbol{F}^k = \boldsymbol{I} + \Delta t \nabla^k \boldsymbol{u}^{k+1} \tag{57}$$

$$= \boldsymbol{I} + \Delta t \nabla^k \boldsymbol{u}^{k'} - \frac{\Delta t^2}{\rho} \nabla^k \left(\nabla^k P\right) \tag{58}$$

Neglecting higher order terms, the equation for pressure in 2D is denoted by

$$\frac{1}{\rho}\left(a_{22}\frac{\partial^2 P^{k+1}}{\partial x^2}+a_{11}\frac{\partial^2 P^{k+1}}{\partial y^2}-(a_{12}+a_{21})\frac{\partial^2 P^{k+1}}{\partial x\partial y}\right)=\frac{1}{\Delta t^2}\left(\det \boldsymbol{A}^k-1\right) \tag{59}$$

$$\boldsymbol{A}^k=\boldsymbol{I}+\Delta t\nabla^k \boldsymbol{u}^{k'}=\begin{pmatrix} a_{11} & a_{12}\\ a_{21} & a_{22}\end{pmatrix} \tag{60}$$

In the practical simulation, however, the volume of the fluid could be increased or decreased. In order to keep the particle volume constant, the incompressible condition from Eq. (55) is altered as follows:

$$\det \boldsymbol{F}^k=\frac{V^{k+1}}{V^k}=\frac{c^k}{c^{k+1}}=c', \tag{61}$$

where c' is defined as:

$$c'=\begin{cases}\max\left(c^k-c_{min}+1, c'_{min}\right) & \left(c^k<c_{min}\right)\\ 1 & \left(c_{min}\le c^k\le c_{max}\right)\\ \min\left(c^k-c_{max}+1, c'_{max}\right) & \left(c_{max}<c^k\right)\end{cases}. \tag{62}$$

Then, Eq. (59) for pressure in 2D is changed accordingly as follows:

$$\frac{1}{\rho}\left(a_{22}\frac{\partial^2 P^{k+1}}{\partial x^2}+a_{11}\frac{\partial^2 P^{k+1}}{\partial y^2}-(a_{12}+a_{21})\frac{\partial^2 P^{k+1}}{\partial x\partial y}\right)=\frac{1}{\Delta t^2}\left(\det \boldsymbol{A}^k-c'\right). \tag{63}$$

This incompressible condition is applied in the Multi-Resolution MPS method. The size of the time step Δt is determined considering the Courant condition:

$$\Delta t\le \min\left(\alpha_C\frac{L_i}{|\boldsymbol{u}_i|}\right). \tag{64}$$

However, if the time step varies for every time step, then the source term in Eqs. (59) and (63) will also vary, which leads to some pressure oscillation. Therefore, a constant time step should be utilised in Eqs. (59) and (63). Note that Eqs. (59) and (63) cannot be employed in the traditional MPS method because each derivative such as $\frac{\partial^2}{\partial x^2}$, $\frac{\partial^2}{\partial y^2}$, $\frac{\partial^2}{\partial x\partial y}$ cannot be calculated separately. This is another advantage of the LSMPS method.

4.4. Multi-resolution techniques

In the Multi-Resolution MPS method, the size of the particles changes dynamically. A particle should be able to be split into smaller particles whenever a more refined resolution is required. Conversely, particles should be able to be merged into a larger particle whenever a coarser particle distribution is required. Splitting and merging are triggered by both the current diameter and a target diameter of each particle. The target diameter L^* can depend on many different parameters such as the position, the distance from a wall, the distance from a free surface, pressure, etc. The easiest way to define the target diameter is to make it to be a function of the coordinates, i.e., $L_i^*=L^*(\boldsymbol{x}_i)$. After evaluating the target diameter for each particle at every time step, then the particle can be judged to be split or merged according to the procedures described in the following sections.

4.4.1. Particle splitting

A particle can be split into any number of particles. If more particles are generated, the diameters after splitting are smaller as shown in Fig. 2. As a result, particles with quite different sizes might exist within the same support domain, which might cause inaccuracy or instability of the method. In terms of accuracy and stability, the difference of diameters between particles should be as small as possible. Therefore, in this work a particle will only be allowed to be split into a maximum of two particles. The particle volume, which is defined by Eq. (26), should be conserved during this particle splitting process, and then the diameter after splitting $L_{i'}$ is given as:

$$L_{i'}=\left(\frac{1}{2}\right)^{\frac{1}{d}}L_i. \tag{65}$$

When the target diameter of a particle is much smaller than the current diameter, i.e. $L_i^*<\beta_s L_i$, the particle will be split. The threshold of the diameter to trigger the particle splitting should be in the middle of the current diameter L_i and the diameter after splitting $L_{i'}$ from Eq. (65), and then the splitting threshold β_s is defined as:

(a) Splitting into 4 particles (b) Splitting into 2 particles

Fig. 2. Particle splitting.

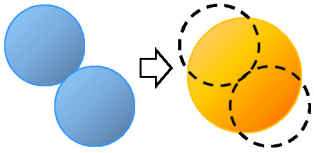

Fig. 3. Particle merging.

$$\beta_s = \frac{1}{2}\left\{\left(\frac{1}{2}\right)^{\frac{1}{d}} + 1\right\}. \tag{66}$$

The position of the particles after splitting $\boldsymbol{x}_{i'}$ is given by:

$$\boldsymbol{x}_{i'} = \boldsymbol{x}_i \pm \frac{\alpha_t}{2} L_{i'} \boldsymbol{t}_i, \tag{67}$$

where $\boldsymbol{t}$ is the direction along which particles are going to be divided. Since splitting into two particles is not isotropic, the splitting direction $\boldsymbol{t}$ should be determined. We defined an error function e_i which, if minimised, would give the best possible splitting direction.

$$e_i = \max\left(e_{ij}\right) \tag{68}$$

$$e_{ij} = \begin{cases} \dfrac{L_{ij} - r_{i'j}}{L_{ij}} & \left(r_{i'j} < L_{ij}\right) \\ 0 & \left(r_{i'j} \geq L_{ij}\right) \end{cases} \tag{69}$$

where $L_{ij} = \frac{L_i + L_j}{2}$ is the average diameter between particle i and j. A smaller error function also means a more uniform particle arrangement. The normalised splitting direction $\boldsymbol{t}$ which delivers the smallest error function within a threshold value $e_i < \alpha_e$ will be chosen. If there is no direction which satisfies the condition above, then the splitting process stops for this particle. Note that if the particle to be split is a free surface particle, then the splitting direction $\boldsymbol{t}$ should be perpendicular to the normal vector $\boldsymbol{n}$, i.e., $\boldsymbol{t} \cdot \boldsymbol{n} = 0$.

The velocity for the new particles after splitting is obtained after the following interpolation:

$$\boldsymbol{u}_{i'} = \boldsymbol{u}_i + \langle \nabla \boldsymbol{u} \rangle_i \left(\boldsymbol{x}_{i'} - \boldsymbol{x}_i\right) \tag{70}$$

4.4.2. Particle merging

Although the arbitrary number of particles can be merged technically, the difference of the diameters during the merging process should be as small as possible for the same reason as the particle splitting process. In this work, therefore, only two particles are allowed to be merged into a large particle as shown in Fig. 3. When the target diameter is much larger than the current diameter, i.e., $L_i^* > \beta_m L_i$, the particle i is merged with a neighbouring particle j. β_m is a merging threshold defined as:

$$\beta_m = 2^{\frac{1}{d}}. \tag{71}$$

Particle j should be of the same kind of fluid as particle i and the distance between particles i and j should be smaller than a pre-defined threshold, i.e., $r_{ij} < \alpha_r \frac{L_i + L_j}{2}$. If there is no neighbouring particle which satisfies the above mentioned condition, then the merging process is terminated. Note that a particle which is going to be split should be ruled out from the merging judgement.

The position and velocity of the newly generated particles after merging are calculated so that the angular momentum and the linear momentum are conserved respectively:

$$\boldsymbol{x}_{i'} = \frac{V_i \boldsymbol{x}_i + V_j \boldsymbol{x}_j}{V_i + V_j} \tag{72}$$

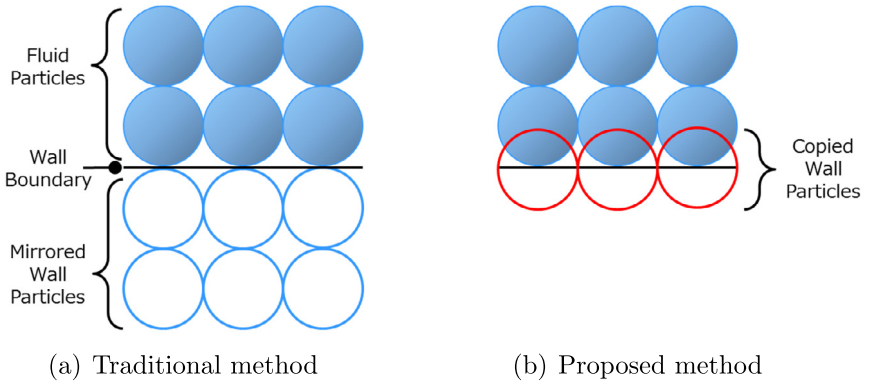

Fig. 4. Imaginary wall particles.

$$\boldsymbol{u}_{i'} = \frac{V_i \boldsymbol{u}_i + V_j \boldsymbol{u}_j}{V_i + V_j} \tag{73}$$

The diameter of the new particle after merging is evaluated by considering volume conservation, i.e.:

$$L_{i'} = \left(L_i^d + L_j^d \right)^{\frac{1}{d}} \tag{74}$$

4.5. Boundary conditions

4.5.1. Wall boundary

Walls are traditionally represented by wall particles which have the main characteristic of being fixed or not moving but instead having pressure values. There has been no special treatment for wall particles and the pressure on wall particles has been calculated in the same manner as for fluid particles. However, this same treatment for wall and fluid particles is only possible to be done for the traditional MPS method adopting the PND condition, in other words, the position based incompressible condition. Note that dummy particles, which have no physical variables, have to be used to calculate the correct particle number density on wall particles. This traditional method might not work well in multi-resolution simulations because of the arbitrary size of particles that can exist around wall particles. As a consequence, smaller fluid particles might leak from larger wall particles when the difference of sizes between fluid particles and wall particles are large enough.

There are some other methods in which walls are represented by polygons (or a group of triangles) so that wall particles can be neglected [9,34,64]. However, these methods are based on the traditional MPS method and they calculate the particle number density of the wall from the distance between a particle and a wall. Therefore these methods cannot be applied to the Multi-Resolution MPS method.

Cummins and Rudman [3] proposed a method to generate imaginary wall particles for the wall boundary by copying fluid particles around the wall to the mirroring position of the wall as shown in Fig. 4(a). Lee et al. [29] used this method and proposed the slip and no-slip boundary conditions by changing the velocity of the imaginary particles. These methods have been widely utilised, however, the Neumann boundary condition for pressure cannot be defined exactly on the wall boundaries [34].

In this paper, wall geometries are represented by polygons and imaginary wall particles are generated on the boundaries at every time step as shown in Fig. 4(b). It would be much easier to impose boundary conditions for the viscosity and pressure terms if the imaginary particles were located right on the boundary because no interpolation technique would then be required for these particles. Note that locating the wall particles right on the wall boundaries is not allowed in the traditional MPS method because the PND incompressible condition would be violated. This arrangement of the wall particles is only possible by the LSMPS method with the velocity-based incompressible condition.

Fluid particles around a wall are copied to generate imaginary wall particles on the boundary. Firstly, the distance from the wall r_{iw}, the normal vector $\boldsymbol{n}_w$ and the curvature σ are calculated for each particle i. If the distance is smaller than a threshold, i.e., $r_{iw} < \alpha_w L_i$, the imaginary particle is then generated. Secondly, the position of the imaginary wall particle $\boldsymbol{x}_{i'}$ is calculated:

$$\boldsymbol{x}_{i'} = \boldsymbol{x}_i - r_{iw} \boldsymbol{n}_w . \tag{75}$$

The diameter of the imaginary wall particle $L_{i'}$ is

$$L_{i'} = \frac{L_i}{1 - r_{iw}\sigma} . \tag{76}$$

Note that the curvature is calculated using the positions $\boldsymbol{x}_1$, $\boldsymbol{x}_2$, $\boldsymbol{x}_3$ and the normal vectors $\boldsymbol{n}_1$, $\boldsymbol{n}_2$, $\boldsymbol{n}_3$ of the nearest triangle:

$$\sigma = -\frac{\sum_{v=1}^{3} w_v \left(\boldsymbol{n}_t - \boldsymbol{n}_v\right) \cdot \left(\boldsymbol{n}_t - \boldsymbol{n}_v\right)}{\sum_{v=1}^{3} w_v \left(\boldsymbol{x}_t - \boldsymbol{x}_v\right) \cdot \left(\boldsymbol{n}_t - \boldsymbol{n}_v\right)} \tag{77}$$

where $\boldsymbol{x}_t = \frac{1}{3}\sum_{v=1}^{3} \boldsymbol{x}_v$ and $\boldsymbol{n}_t = \frac{1}{3}\sum_{v=1}^{3} \boldsymbol{n}_v$ are the average position and the average normal vector respectively.

The boundary condition on the wall particles is defined as follows:

$$\boldsymbol{u}^{k+1} \cdot \boldsymbol{n} = 0\Big|_{\Gamma}. \tag{78}$$

There are various ways to express the pressure boundary condition on wall particles. Adami et al. [1] and Valizadeh and Monaghan [60] formulated the pressure for the wall particles as:

$$P_i = \frac{\sum_j P_j W_{ij} + (\boldsymbol{f} - \boldsymbol{a}_i) \cdot \sum_j \rho_j \boldsymbol{x}_{ij} W_{ij}}{\sum_j W_{ij}}. \tag{79}$$

Guermond et al. [8] have reviewed a few projection schemes and analysed the consistency of the pressure gradient on the wall. They have stated that the rotational pressure-correction scheme [58], as shown below, provides the required consistency for the pressure on the wall particles:

$$\begin{cases} \dfrac{1}{2\Delta t}\left(3\boldsymbol{u}_{k'} - 4\boldsymbol{u}_k + \boldsymbol{u}_{k-1}\right) = -\dfrac{1}{\rho}\nabla P^k + \nu\nabla^2 \boldsymbol{u}^{k'} + \boldsymbol{f}, \qquad \boldsymbol{u}^{k'}\Big|_{\Gamma} = 0 \\ \dfrac{1}{2\Delta t}\left(3\boldsymbol{u}^{k+1} - 3\boldsymbol{u}^{k'}\right) = -\dfrac{1}{\rho}\nabla\left(P^{k+1} - P^k + \mu\nabla\cdot\boldsymbol{u}^{k'}\right) \end{cases} \tag{80}$$

This rotational scheme has been utilised successfully [12]. Tamai and Koshizuka [52] have generalised the rotational scheme as shown below.

$$\begin{cases} \dfrac{1}{\Delta t}\left(\boldsymbol{u}_{k'} - \boldsymbol{u}_k\right) = -\dfrac{1}{\rho}\nabla P^* + \nu\nabla^2 \boldsymbol{u}^{k'} + \boldsymbol{f}, \qquad \boldsymbol{u}^{k'}\Big|_{\Gamma} = 0 \\ \dfrac{1}{\Delta t}\left(\boldsymbol{u}^{k+1} - \boldsymbol{u}^{k'}\right) = -\dfrac{1}{\rho}\nabla\left(P^{k+1} - P^* + \chi\mu\nabla\cdot\boldsymbol{u}^{k'}\right) \end{cases} \tag{81}$$

where P^* is a generalised pressure prediction e.g. $P^* = 0, P^k, 2P^k - P^{k-1}, \cdots$ and $\chi = 0$ or 1 is a user defined parameter. According to Tamai and Koshizuka [52], using $\chi = 0$ leads to an inconsistent pressure boundary condition while $\chi = 1$ leads to a consistent condition. However, this parameter χ is just changing the way of calculating the viscosity term and it has no influence on the pressure boundary. It is not the parameter χ but the pressure prediction P^* that affects the consistency of the pressure: the pressure boundary is inconsistent if $P^* = 0$ and consistent otherwise.

The pressure predictor term P^* is not employed in this work in order to simplify the simulation process, another consistent approach is needed. Leroy et al. [30] have proposed a semi-analytical wall boundary condition which is directly derived from Eq. (78).

$$\left(\boldsymbol{u}^{k'} - \frac{\Delta t}{\rho}\nabla P\right)\cdot\boldsymbol{n} = 0\Big|_{\Gamma} \tag{82}$$

$$\Leftrightarrow \frac{1}{\rho}\nabla P\cdot\boldsymbol{n} = \frac{1}{\Delta t}\boldsymbol{u}^{k'}\cdot\boldsymbol{n}\Big|_{\Gamma} \tag{83}$$

The velocity of the wall is evaluated by using the velocities of the neighbouring particles. Although the LSMPS type B can be used to extrapolate the velocity, extrapolation by the LSMPS type B can sometimes cause locally higher pressure when the velocity difference around the wall is large enough. Therefore, averaging the velocities of neighbouring particles is recommended for more stable simulations. Even though this more stable extrapolation is applied, some wall particles are likely to have extraordinary pressure values compared with the pressure values of the neighbouring wall particles. This is because this boundary condition considers the component in the normal direction only. To smooth the pressure distribution and improve stability, the pressure gradient in the tangential direction $\boldsymbol{t}$ (s.t. $\boldsymbol{n}\cdot\boldsymbol{t} = 0$) should be smaller, e.g. $\nabla P\cdot\boldsymbol{t} = 0$. Combining with Eq. (83), a new boundary condition for wall is derived:

$$\frac{1}{\rho}\left(\nabla P\cdot\boldsymbol{n} + \nabla P\cdot\boldsymbol{t}\right) = \frac{1}{\Delta t}\boldsymbol{u}^{k'}\cdot\boldsymbol{n}\Big|_{\Gamma} \tag{84}$$

Although this does not strictly impose the wall boundary condition expressed by Eq. (78), a smoother pressure distribution can however be obtained for the wall particles.

The standard LSMPS type A can be applied to calculate the gradient of the pressure ∇P for wall particles, however, some errors might occur due to the lack of sufficient neighbouring particles near the wall. Another LSMPS formulation considering the Neumann boundary condition has been proposed by Tamai and Koshizuka [52], which is going to be used in this work. A derivative operator $\boldsymbol{D}_{\boldsymbol{x}}$ is re-written as:

$$\boldsymbol{D}_{\boldsymbol{x}} f(\boldsymbol{x})|_{\boldsymbol{x}_i} = \boldsymbol{H}_i \left[[\boldsymbol{M}_i + \boldsymbol{N}_i]^{-1} \{\boldsymbol{b}_i + \boldsymbol{c}_i\} \right]\Big|_{\Gamma}, \tag{85}$$

$$\boldsymbol{N}_i = w(0)\, \boldsymbol{p}(-\boldsymbol{n}_i) \otimes \boldsymbol{p}(-\boldsymbol{n}_i), \tag{86}$$

$$\boldsymbol{c}_i = w(0)\, \boldsymbol{p}(-\boldsymbol{n}_i)\, \nabla f \cdot (-L_i \boldsymbol{n}_i). \tag{87}$$

In order to fulfil the no-slip condition for the viscosity term, it has been common practice to correct the velocity term for wall particles [33,1,60], e.g. $\boldsymbol{u}_i = 2\boldsymbol{u}_j - \sum_j \boldsymbol{u}_j W_{ij} / \sum_j W_{ij}$. The reason why such a velocity correction has been needed is due to the wall particles not being located on the boundary. Since the wall particles are located right on the boundary in the proposed method, there is no extra handling necessary for this procedure.

4.5.2. Pressure boundary

When flows inside channels are simulated, some boundary conditions such as inflow and outflow are commonly used in particle methods [28]. Normally, the velocity is fixed at the inflow boundary and particles are generated every time they go forward over a specific distance. There is no special treatment except to remove particles which are beyond the simulation domain in the traditional outflow boundary. Shibata et al. [49] proposed a new outflow boundary condition to keep the number of particles in the simulation domain constant by enforcing the velocity at the outflow region. In the LSMPS method, however, the fixed velocity in the boundary might cause inconsistency in the velocity field because pressure is calculated from the velocity field. Therefore, a pressure boundary, in which the pressure is fixed and the velocity is variable, is preferable. However, in the authors' knowledge, there is no pressure boundary condition proposed so far for particle methods, although pressure boundary conditions have been commonly used for Eulerian methods. Therefore, a new method to impose the pressure boundary condition is proposed in this paper.

Particles for the pressure boundary are located right on the pressure boundary (similar as the location for wall particles from Fig. 4(b)). Particles for the pressure boundary can be arranged in advance, or can be generated by duplicating neighbouring particles at every time step in a procedure similar as the one used for the wall boundary. The Dirichlet boundary condition can then be imposed onto these pressure boundary particles.

The particles on pressure boundaries can have arbitrary velocities, which means inflow or outflow can take place at these boundaries. If the velocity of a pressure boundary particle p is towards outside direction, i.e. $\boldsymbol{u}_{i\in\mathcal{P}} \cdot \boldsymbol{n}_p < 0$, then outflow takes place. When the distance between a particle i and a pressure boundary particle p is small enough, i.e. $r_{ip} < \alpha_o L_i$, then particle i is discarded from the simulation domain.

On the contrary, if the velocity of a pressure boundary particle p is towards inside direction, i.e. $\boldsymbol{u}_{i\in\mathcal{P}} \cdot \boldsymbol{n}_p > 0$, then inflow takes place. The inflow position is given by $\boldsymbol{x}_I = \boldsymbol{x}_P + \alpha_i \boldsymbol{n}_P$. If there is no particle at the inflow position, i.e. $\forall i \in \mathcal{F} : |\boldsymbol{x}_I - \boldsymbol{x}_i| > \alpha_I L_i$, a new particle is generated at location $\boldsymbol{x}_I$. The velocity of this new particle is interpolated using the LSMPS type B. Note that the velocity on the pressure boundary should have the same direction as the normal vector of the pressure boundary for stability purposes.

4.6. Surface detection

Surface detection is quite important for simulations of flows with free surfaces. In the traditional MPS method, Eq. (20) is commonly used for surface detection. Tanaka and Masunaga [55] used the number of neighbouring particles instead of the particle number density for surface detection. However, these density-based detection methods are not accurate even for single resolution simulations.

Geometry-based detection methods, such as the arc method [5], are considered to be more reliable. Shibata et al. [48] developed a similar methodology as the arc method and extended it into three dimensions. Tamai and Koshizuka [52] proposed a geometry-based surface detection method by checking if there exists any particle along the normal direction. This method works well in a single resolution simulation, however, in some multi-resolution cases some particles on the surface are mistakenly judged to be inside particles especially when they are located near a wall.

In this work, geometry-based methods are extended for the Multi-Resolution MPS method. Firstly, isolated particles are detected by using the following condition: $c_i < \alpha_c$. These isolated particles are neglected from the calculation of the Navier–Stokes equation (except for the external forces) and their motion follows the Newton's second law or the equation of motion. Note that these isolated particles don't interact with any other particles and don't interfere in the surface detection process as well.

In the second step, the number of neighbouring particles N_θ within a specific angle θ are calculated from the following conditions:

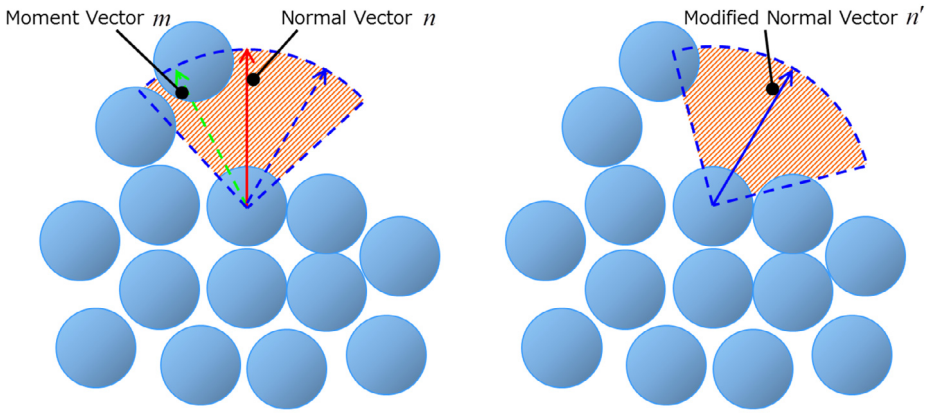

Fig. 5. Surface detection.

$$\left|\boldsymbol{x}_{ij}\right| < \alpha_\theta L_i \wedge \boldsymbol{n}_i \cdot \frac{\boldsymbol{x}_{ij}}{\left|\boldsymbol{x}_{ij}\right|} > \cos\theta_1 \tag{88}$$

where $\theta_1 = \pi/4$. If $N_\theta = 0$, this particle is then considered to be a surface particle. This procedure is schematically described in Fig. 5(a). Sometimes the normal vector $\boldsymbol{n}$ does not have an appropriate direction for surface detection and therefore a third step is required for a proper judgement of additional surface particles to be added.

In the third step, the normal direction is modified and the same particle count is conducted as shown in Fig. 5(b). The modified normal direction $\boldsymbol{n}_i' = 2\left(\boldsymbol{m}_i \cdot \boldsymbol{n}_i\right)\boldsymbol{n}_i - \boldsymbol{m}_i$ is calculated using the moment vector $\boldsymbol{m}_i = \sum_{j\neq i}\boldsymbol{x}_{ij} / \left|\sum_{j\neq i}\boldsymbol{x}_{ij}\right|$ where the neighbour particle j to be considered is such that $\boldsymbol{n}_i \cdot \boldsymbol{x}_{ij} > \left|\boldsymbol{x}_{ij}\right|\cos\theta_2$, where $\theta_2 = \pi/2$. Then the number of neighbouring particles N_θ' s.t.

$$\left|\boldsymbol{x}_{ij}\right| < \alpha_\theta L_i \wedge \boldsymbol{n}_i' \cdot \frac{\boldsymbol{x}_{ij}}{\left|\boldsymbol{x}_{ij}\right|} > \cos\theta_1 \tag{89}$$

is counted and if $N_\theta' = 0$, the particle i is detected as a surface particle. Remaining particles are judged to be inside particles. Note that the surface state of an imaginary wall particle is the same with the original particle before being copied.

4.7. Particle shifting

The LSMPS method does not require most of the stabilisation techniques usually required for the traditional MPS scheme, such as the ones based on the negative pressure correction and on the altering the formulation for the pressure gradient term. However, it is well-known that a Lagrangian method must experience particle clustering in some cases no matter how accurate the method is [42].

The collision model [29] is useful for the stabilisation of the traditional MPS method, however, this method does not work well with the LSMPS method. The main reason is the velocity field which changes due to particle collisions and therefore the pressure field cannot be calculated correctly from velocity-based incompressible conditions.

The particle shifting method by Xu et al. has been proposed to overcome or avoid the particle clustering [61]. In particle shifting, the position of a particle is slightly altered as follows:

$$\delta\boldsymbol{x} = C_{Shift} R^2 \nabla C \tag{90}$$

where C is the concentration defined as $C_i = \sum_j V_j w_{ij}$. If all particles have the same diameter, this concentration can then be replaced by the particle number density. The velocity is interpolated by first order Tailor Series Expansion:

$$\delta\boldsymbol{u} = \nabla\boldsymbol{u}\delta\boldsymbol{x} \tag{91}$$

Oger el al. [42] proposed a new method to calculate the new velocity more accurately by using Arbitrary Lagrangian–Eulerian (ALE) formulations. Khayyer et al. [19] proposed another correction technique by optimising particle shifting around free surfaces, with the new position being given by:

$$\delta\boldsymbol{x} = -C_{Shift} R^2 \left(\boldsymbol{I} - \boldsymbol{n}\otimes\boldsymbol{n}\right)\nabla C \tag{92}$$

Mokos et al. [36] extended the particle shifting algorithm to a multi-phase simulation.

A similar approach can be formulated by using the packing ratio c instead of the concentration C, however, the spatial distribution for the packing ratio c is not always smooth in the multi-resolution simulations. Therefore, a new particle shifting is proposed for the Multi-Resolution MPS method. The primal particle displacement is given by the following equation:

$$\delta \boldsymbol{x}^* = \begin{cases} \boldsymbol{g}_i - \boldsymbol{x}_i & \left(\left|\boldsymbol{g}_i - \boldsymbol{x}_i\right| > \alpha_g L_i\right) \\ 0 & \left(\left|\boldsymbol{g}_i - \boldsymbol{x}_i\right| \leq \alpha_g L_i\right) \end{cases} \tag{93}$$

where $\boldsymbol{g}$ is the centre of mass, which is defined as follows:

$$\boldsymbol{g}_i = \frac{\sum_{j \neq i} w_{ij} \left(\boldsymbol{x}_j + r^*_{ij} \frac{\boldsymbol{x}_{ji}}{|\boldsymbol{x}_{ji}|} \right)}{\sum_{j \neq i} w_{ij}} \tag{94}$$

where r^*_{ij} is the target distance, which is defined by using the averaged particle diameter $L_{ij} = \frac{L_i + L_j}{2}$ as follows:

$$r^*_{ij} = \begin{cases} L_{ij} & \left(r_{ij} \leq \alpha_T L_{ij}\right) \\ \dfrac{R_{ij} - L_{ij}}{R_{ij} - \alpha_T L_{ij}} \left(r_{ij} - \alpha_T L_{ij}\right) + L_{ij} & \left(r_{ij} > \alpha_T L_{ij}\right). \end{cases} \tag{95}$$

This procedure for the particle shifting only works when the distance between the particle position and the centre of mass is larger than the threshold $\alpha_g L_i$ as expressed in Eq. (93). In other words, this technique for the particle shifting is not used regularly but it needs to be considered exceptionally in order to prevent particle clustering. The displacement is calculated based on the separation movement between each neighbouring particle. Therefore, this method for the particle shifting might not work well for the particles around surfaces or boundaries and sometimes it can lead to particle overlapping. In order to overcome the particle overlapping effect, another technique for the particle shifting was developed and used in our analysis. The new particle shifting is obtained from the following expression:

$$\delta \boldsymbol{x}^{**}_i = -\sum_{j \neq i} w_{ij} \epsilon_{ij} \frac{\langle \nabla c \rangle_i}{|\langle \nabla c \rangle_i|} \tag{96}$$

where ϵ is a penalty function defined as:

$$\epsilon_{ij} = \begin{cases} \dfrac{\left(1 - \alpha_p\right) L_{ij} - r_{ij}}{L_{ij}} & \left(r_{ij} < \left(1 - \alpha_p\right) L_{ij}\right) \\ 0 & \left(r_{ij} \geq \left(1 - \alpha_p\right) L_{ij}\right). \end{cases} \tag{97}$$

Then, the final displacement is:

$$\delta \boldsymbol{x}_i = \delta \boldsymbol{x}^*_i + \delta \boldsymbol{x}^{**}_i. \tag{98}$$

The displacements for the free surface particles and for the particles around boundaries are altered according to the Optimised Particle Shifting method [19] by neglecting the normal component:

$$\delta \boldsymbol{x}_i|_S = \left(\boldsymbol{I} - \boldsymbol{n}_i \otimes \boldsymbol{n}_i\right) \delta \boldsymbol{x}_i \tag{99}$$

It is not desirable if the displacement by the particle shifting is large when compared with that by the advection because the particle distribution changes significantly. Therefore the displacement by the particle shifting is limited in this work:

$$|\delta \boldsymbol{x}_i| \leq \alpha_S L_i \tag{100}$$

The velocity is interpolated as well as the standard particle shifting.

5. Results and discussions

5.1. Verification of differential operators in multi-resolution particle arrangement

The accuracy of the differential operators for the LSMPS method in multi-resolution particle arrangements is verified. The utilised particle arrangement is depicted in Fig. 6. Smaller particles are located in the region of $x < 0$ and larger particles are in the region of $x > 0$. Five different particle arrangements are utilised where the size difference between smaller and larger particles is varied. The diameter of smaller particles is fixed to 1.0 and the diameter of larger particles varies within the following set of diameters: 1.0, 1.5, 2.0, 2.5 and 3.0.

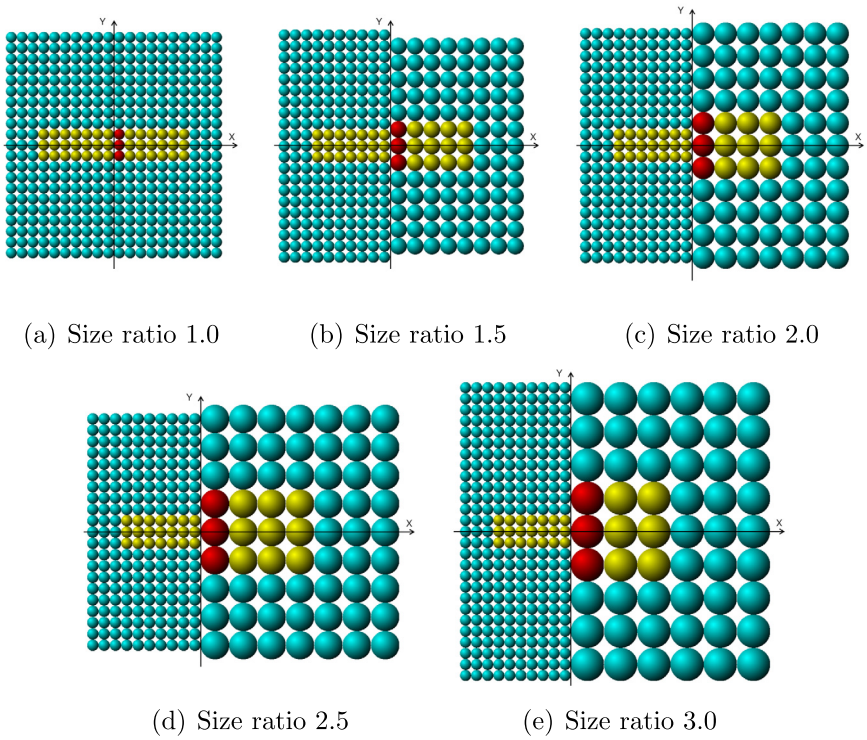

Fig. 6. Particle arrangement for verification. (For interpretation of the references to colour in this figure, the reader is referred to the web version of this article.)

Table 1
List of coefficients for verification of differential operators.

a	b	c	d	e	f
−9.97681	−5.28855	2.96304	−8.51253	−4.59517	−2.79946
−4.89425	9.70580	−3.62163	8.68465	−6.42750	7.15140
−9.30296	−9.82849	2.53517	−0.28230	−4.54024	6.04358
−8.17072	−1.03977	2.80313	9.46532	3.21757	5.81225
1.26560	−9.19248	7.62810	−8.63277	−4.06415	9.70153
−8.50703	−9.63988	−9.48729	1.34495	0.31953	2.96243
4.41145	−2.29896	−2.39723	−9.47081	8.02606	−5.80187
7.22648	0.91769	9.28587	2.56386	−2.54616	8.98923
−5.37461	0.41658	−5.34349	7.94733	−2.50526	−1.75695
4.88571	−2.88980	−2.47475	−5.61998	−8.57723	1.75817

The following reference analytical function is given for each particle:

$$f(x) = ax^2 + by^2 + cxy + dx + ey + f \tag{101}$$

where coefficients a, b, c, d, e, f are generated from the use of random numbers. The gradient elements $\frac{\partial f}{\partial x}$, $\frac{\partial f}{\partial y}$ and Laplacian $\frac{\partial^2 f}{\partial x^2} + \frac{\partial^2 f}{\partial y^2}$ are evaluated on the yellow and red particles from Fig. 6 by using both the LSMPS and the MPS methods. The computed gradient and Laplacian are compared with the analytical values $\frac{\partial f}{\partial x} = 2ax + cy + d$, $\frac{\partial f}{\partial y} = 2by + cx + e$, $\frac{\partial^2 f}{\partial x^2} + \frac{\partial^2 f}{\partial y^2} = 2a + 2b$. Ten calculations using ten different functions are conducted for each particle arrangement. The utilised values of the coefficients are shown in Table 1.

We define the accuracy as ϕ_c/ϕ_a, where ϕ_c is the computed value and ϕ_a is the analytical value, and the differential operator is completely accurate if the accuracy has the value of 1. The accuracy of $\frac{df}{dx}$ when the size ratio is 1.0, 1.5, 2.0 and 3.0 is plotted in Fig. 7. When the diameters of all particles were the same, both the LSMPS and the MPS methods are able to provide accurate results as shown in Fig. 7(a). On the other hand, when there are different sizes of particles, in other words, in a multi-resolution particle arrangement, the traditional MPS tends to lose its accuracy while the LSMPS method remains accurate. Note that similar results were observed for the other differential operators.

The relationship between size ratio and accuracy for the red particles in Fig. 6 is investigated since the accuracy is likely to get worse for the interfacial particles. The results are illustrated in Fig. 8. The LSMPS method is accurate for any size

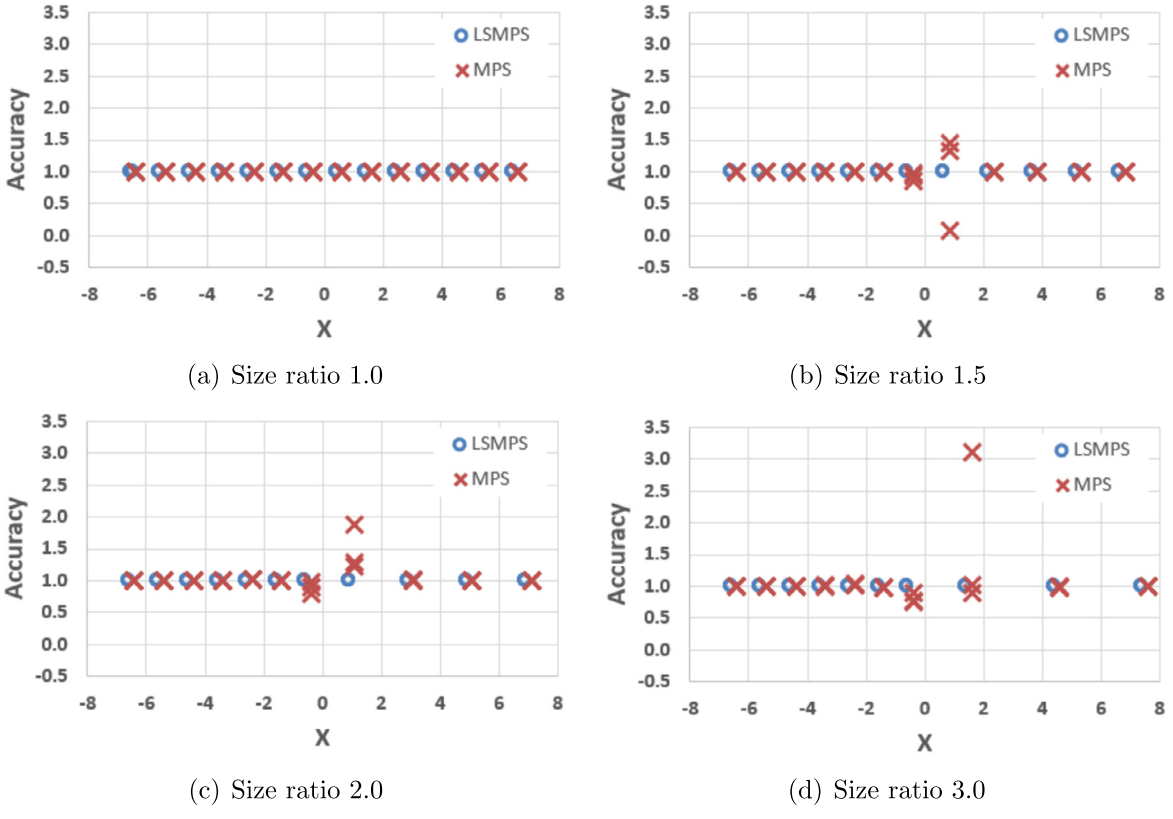

(a) Size ratio 1.0

(b) Size ratio 1.5

(c) Size ratio 2.0

(d) Size ratio 3.0

Fig. 7. Accuracy of $\frac{df}{dx}$.

ratio while the accuracy of the MPS method gets worse for higher size ratios. These results suggest that the traditional MPS method cannot be applied to a multi-resolution simulation unless the formulations for the derivative operators are corrected. On the other hand, the LSMPS method can provide accurate results even in a multi-resolution simulation scheme. Note that although the 2nd order LSMPS scheme was employed in these examples, other schemes with an arbitrary order can be utilised depending on simulation conditions.

5.2. Poiseuille flow simulation with multi-resolution particle arrangement

In this section, flow simulations in a pipe channel with constant diameter, also known as the Poiseuille flow, are conducted. The geometry of the pipe is illustrated in Fig. 9. The pipe has a diameter of 10 mm and length of 100 mm. The newly proposed pressure boundaries from section 4.5.2 are imposed on the left and right surfaces and the pressure values used are 100 Pa and 0 Pa, respectively. In this example, the left boundary works as an inflow boundary and the right boundary as an outflow boundary, although the inflow and outflow conditions are not configured explicitly in advance. No external force is considered. The density is 1000 kg/m^3 and the viscosity is 0.1 Pa s. Two simulations with different sizes of particles are conducted: the single resolution simulation with the diameter of 0.125 mm and the multi-resolution simulation with the diameters ranging from 0.125 mm around the wall and 0.5 mm in the centre of the channel. The number of particles for the initial state was 65,870 for the single resolution simulation while it was 26,708 for the multi-resolution simulation.

The obtained velocity fields of the two simulations are shown in Fig. 10. The velocities were varied only in the cross sectional direction in both simulations. Note that the spatial resolution is not changed dynamically in the multi-resolution simulation since no particle moves in the cross sectional direction and all particles stay in the same resolution region throughout the simulation. In other words, the number of particles used in the simulation was able to be reduced by 59.4% throughout the simulation. Additionally, the time step for the multi-resolution simulation, which is determined by the Courant condition from Eq. (64), was about twice larger than that for the single resolution simulation because the larger particles were located in the higher velocity region. As a result, the computational time was able to be reduced by 86.0% by using the multi-resolution discretisation.

The velocities are evaluated at the points in the middle of the pipe as shown in Fig. 9, and the comparison with the theoretical values is shown in Fig. 11. Both results of the single and multi-resolution simulations are in very good agreement with the theoretical values even though the multi-resolution simulation required less computational resources as described

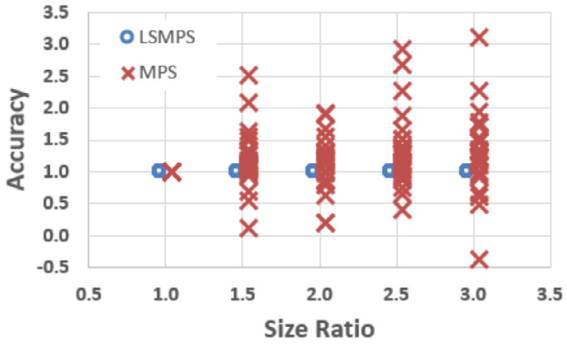

(a) $\frac{df}{dx}$

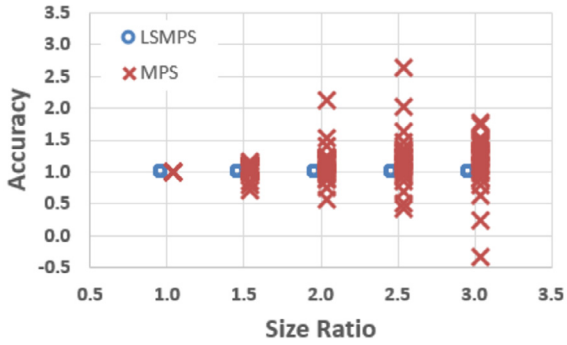

(b) $\frac{df}{dy}$

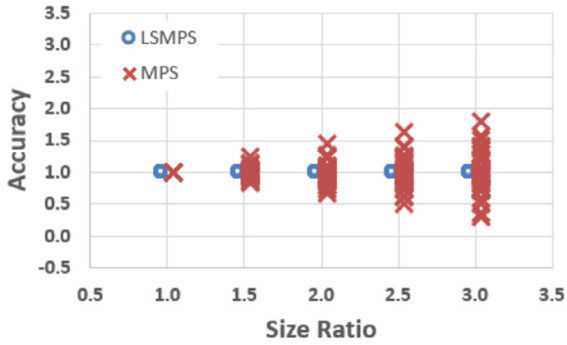

(c) Laplacian

Fig. 8. Accuracy of derivatives versus size ratio.

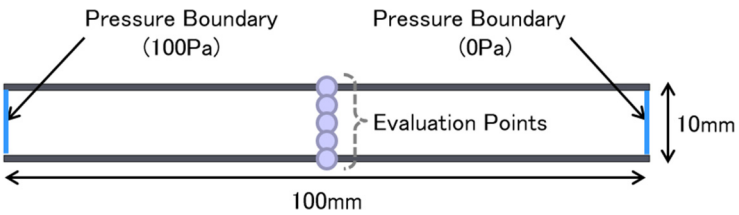

Fig. 9. Simulation condition of the Poiseuille flow.

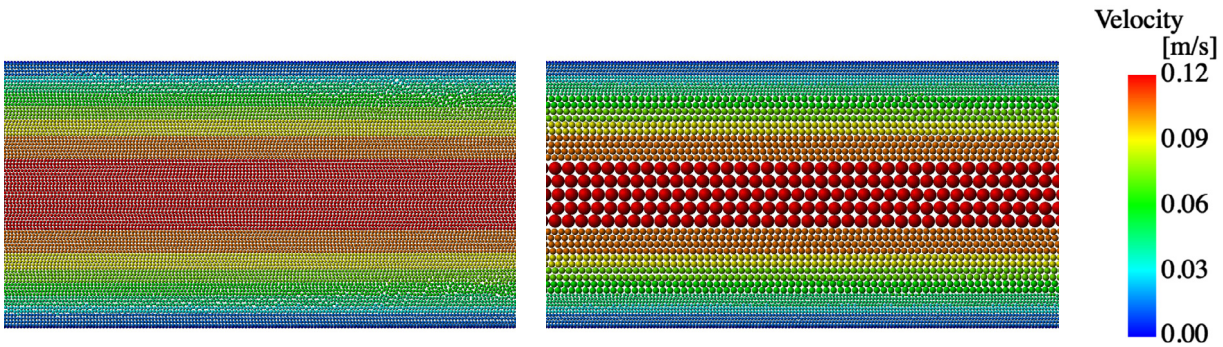

(a) Single resolution (b) Multi-resolution

Fig. 10. Simulation results of the Poiseuille flow.

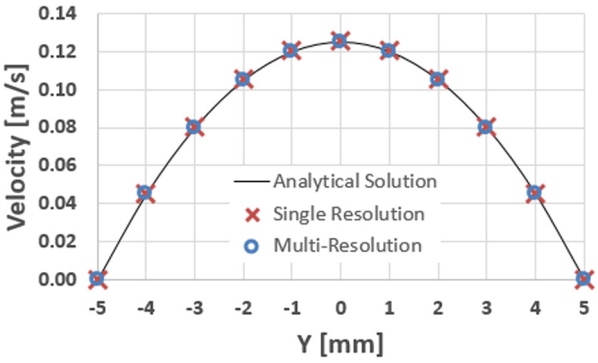

Fig. 11. Velocity distribution in the Poiseuille flow simulations.

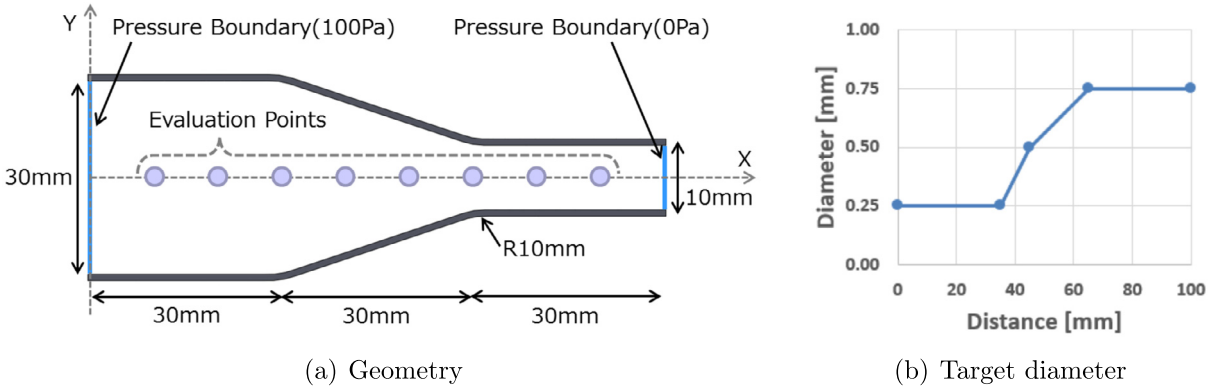

Fig. 12. Simulation condition of the multi-diameter channel.

above. This result indicates that the multi-resolution technique is supposed to be able to be applied to boundary layer simulations, which has hardly been simulated with a particle method because of the limitation of the spatial resolution.

5.3. Multi-diameter channel simulation with particle splitting

A flow in a multi-diameter channel is simulated in this section. The geometry of the simulation is shown in Fig. 12(a). The channel has a diameter of 30 mm on the left hand side and a diameter of 10 mm on the right hand side of the channel. The total length of the multi-diameter channel is 90 mm and each section of the channel (wide, transitional and narrow sections) have the same length of 30 mm. The pressure boundaries are imposed on the left and right sides of the channel, with the values for the pressure being 100 Pa and 0 Pa, respectively. The fluid flows in from the left boundary and it flows out of the right boundary. The density used in the simulation is 1000 kg/m^3 and the dynamic viscosity is 0.001 Pa s. No external force is considered in the analysis. A single resolution simulation with the particle diameter of 0.25 mm and a multi-resolution simulation with the diameter ranging from 0.25 mm to 0.75 mm are conducted. The target diameter in the multi-resolution simulation depends on the distance from the mid point of the right hand side boundary as shown in Fig. 12(b).

The diameter distribution after the simulation of 1.0 s is illustrated in Fig. 13. Larger particles are located on the wider section of the channel and smaller particles are located on the narrower section of the channel. Even after the simulation proceeded and particles moved from left to right, the diameter distribution was almost the same. This is because the larger particles were split into two smaller particles properly. The closeup images in Fig. 13 show that the spatial resolution was changed without any unnatural particle clustering and they also show that the resolution of wall particles changed adaptively.

The velocity fields at the time of 1.0 s obtained for both the single and multi-resolution simulations are illustrated in Fig. 14. The contours represent the velocity in the direction of the X axis. The velocity is smaller in the wider part on the left side of the channel, on the other hand, it is larger in the narrower section located on the right side of the channel. The velocity fields of the single and multi-resolution simulations were similar especially for the high resolution region. Some differences which are seen around the wall of the wider part are due to the difference of the resolution employed. Note that the velocity around the left pressure boundary, which worked as an inflow boundary, was not constant and particles with various velocities flowed into the domain. This is one of the differences between the proposed pressure boundary condition and the traditional inflow boundary condition, in which the constant velocity is defined.

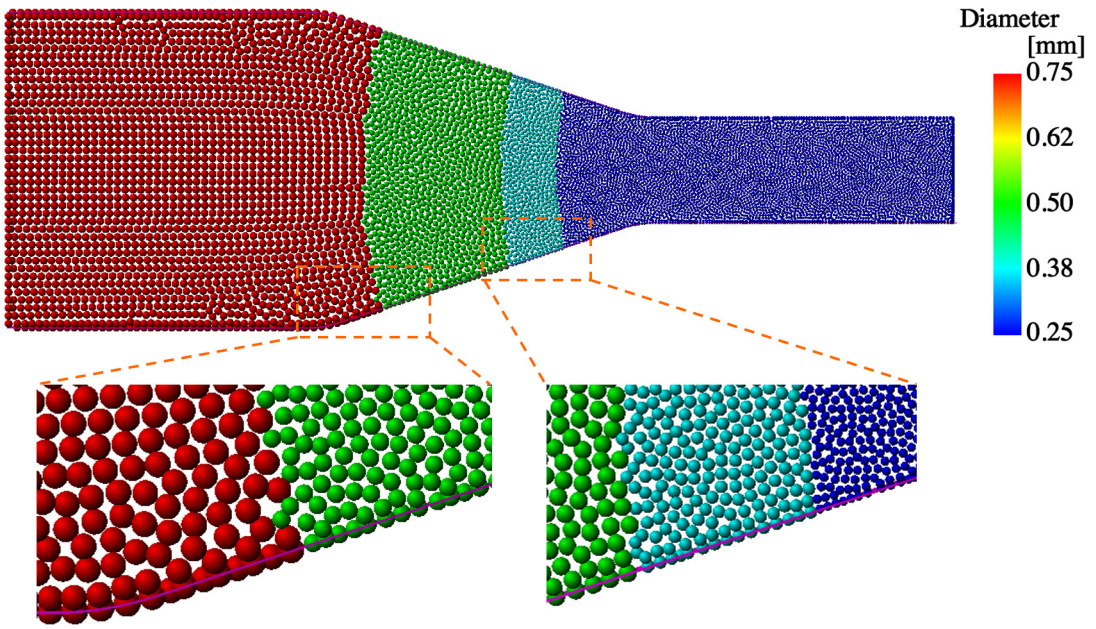

Fig. 13. Diameter distribution in the multi-diameter channel simulation.

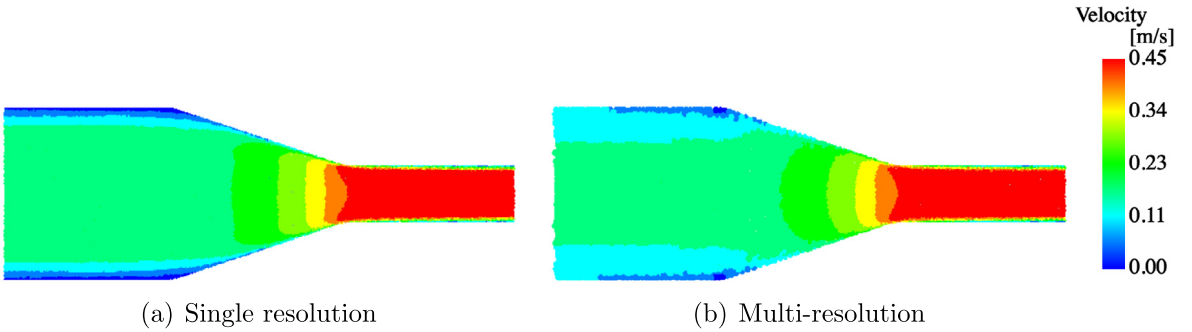

Fig. 14. Velocity distribution in the multi-diameter channel simulation.

The quantitative verification was conducted by comparing the results of the proposed method with that of FLUENT. The comparison of velocities and pressures are shown in Fig. 15(a) and Fig. 15(b) respectively. All of the results from FLUENT, the single resolution simulation and the multi-resolution simulation, were in good agreement and it was shown that the particle splitting process worked well without any instability or inaccuracy.

The average number of particles used in the single resolution simulation was 29,448 while it was 10,481 in the multi-resolution simulation. This corresponds to a reduction of 64.4% in the number of particles and a reduction of 75.8% in the computational time by using the multi-resolution techniques.

5.4. Taylor Green vortex simulation with variable resolution

The Taylor Green vortex example is simulated with the Multi-Resolution MPS method for the assessment of the conservation of energy and momentum. The Taylor Green vortex is a classical flow example with known analytical solution. The velocity $\boldsymbol{u}(x, y, t) = (u(x, y, t), v(x, y, t))$ and pressure $P(x, y, t)$ are expressed by using the coefficient $F(t) = U \exp(-2\nu t)$ as follows:

$$u(x, y, t) = F(t) \cos\left(2\pi \frac{x}{W}\right) \sin\left(2\pi \frac{y}{W}\right) \tag{102}$$

$$v(x, y, t) = -F(t) \sin\left(2\pi \frac{x}{W}\right) \cos\left(2\pi \frac{y}{W}\right) \tag{103}$$

$$P(x, y, t) = -\frac{\rho F(t)^2}{4} \left\{\cos\left(4\pi \frac{x}{W}\right) + \cos\left(4\pi \frac{y}{W}\right)\right\} \tag{104}$$

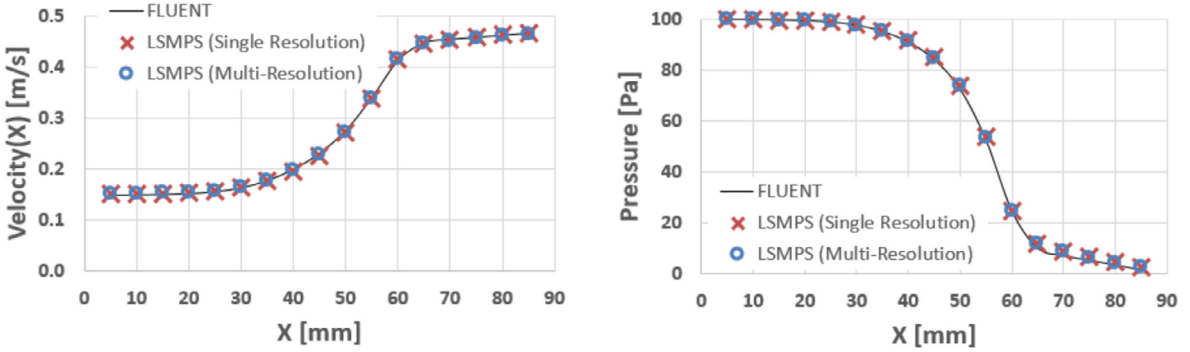

Fig. 15. Comparison of velocity and pressure with FLUENT.

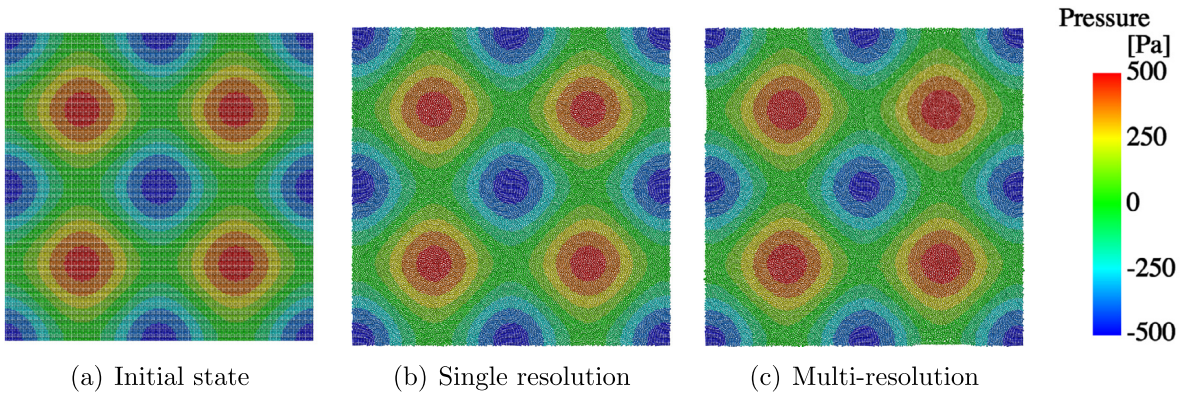

Fig. 16. Pressure distribution of the Taylor Green vortex simulations.

where W is the size of the domain so that the coordinates are limited to $0 \leq x \leq W$ and $0 \leq y \leq W$, and U is the reference velocity.

The domain size used in the simulations was $W = 1$ m and the reference velocity was $U = 1$ m/s. The fluid density was 1000 kg/m^3 and the kinematic viscosity was 0 m^2/s. Because the viscosity term is neglected, the velocity and pressure distribution should remain still and the energy should be conserved. The particles whose diameters are 5 mm are located on the 200 $\times$ 200 grids in the initial state for both single and multi-resolution simulations. In the multi-resolution simulation, the region within 0.25 m distance to the point (0.75 m, 0.75 m) is defined as the high resolution region, and the target diameter of the particles inside this region is 0.35 m. The simulations were conducted for a total time of 1.0 s, which corresponds to one cycle for the vortex. The periodic boundary conditions are applied for X and Y directions by copying particles around edges of the simulation domain to the corresponding positions of the periodic boundary condition.

The pressure distribution and the velocity distribution before and after simulations are shown in Fig. 16 and Fig. 17 respectively. The distributions of the pressure and the velocity after both single and multi-resolution simulations are similar to the initial state although particles have moved for the time corresponding to one cycle of the vortex, and then it can be stated that the simulation was conducted accurately. The closeups of the regions where the resolution was changed are shown in Fig. 18. In the left closeup, particles are moving from left to right direction and they are split when they enter the high resolution region. In the right closeup particles are moving from up to down direction and are merged whenever they get out of the high resolution region. In both the splitting and merging process, the velocity field was smooth and no strange particle arrangement was observed.

The pressure and velocity were measured on the evaluation points, shown in Fig. 18, along the vertical line corresponding to $X = 0.75$ m and they were plotted together with the analytical solutions in Fig. 19. The results of both of the single and multi-resolution simulation were in good agreement with the analytical solutions although there was a slight difference for the pressure of the multi-resolution simulation around $Y = 0.5$ m. This point is near the interfacial region of the different size of particles and the error was supposed to be caused by changing the resolution. However the difference was small enough and did not affect the accuracy of the whole simulation.

The linear and angular momentum and the total energy through the simulations were monitored in Fig. 20. The errors for the momentum from the multi-resolution simulation were larger than those from the single resolution simulation although they are not significant. The error for the energy was as small as 0.1% and thus it can be said that the accuracy of the

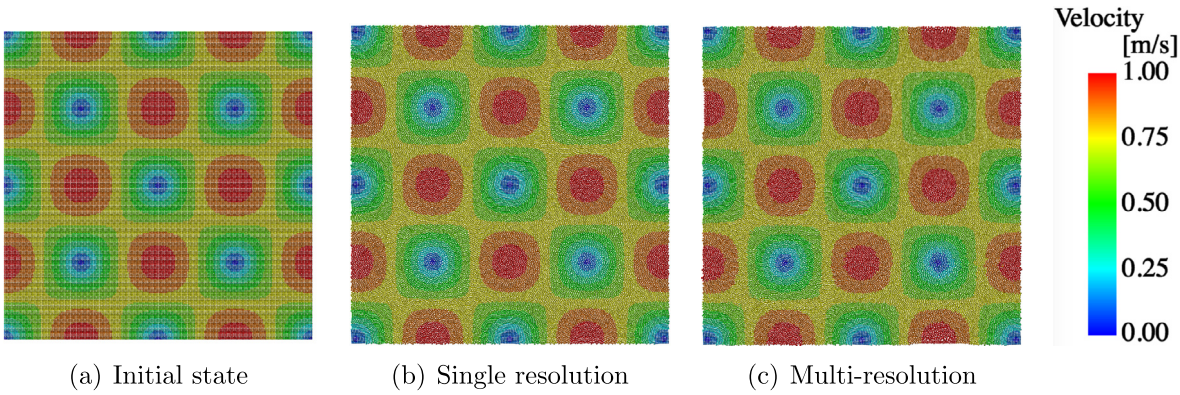

Fig. 17. Pressure distribution of the Taylor Green vortex simulations.

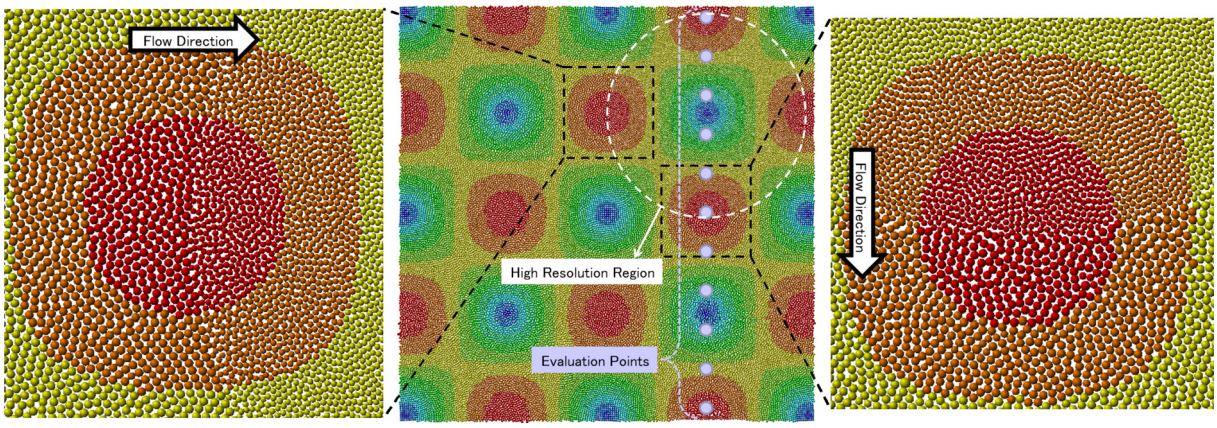

Fig. 18. Closeups of resolution changing regions.

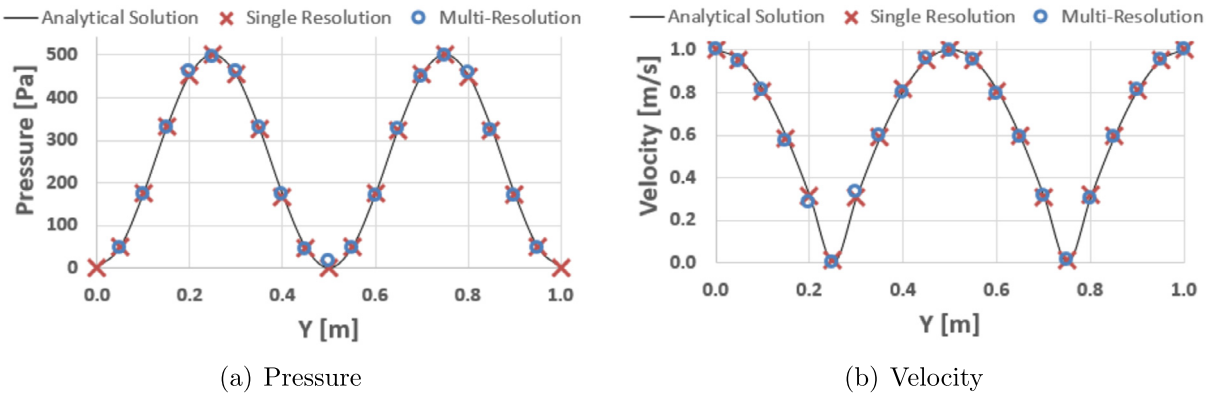

Fig. 19. Comparison between the analytical solution and the simulation results.

Multi-Resolution MPS method is good enough so that the method can be successfully applied in the simulation of complex problems.

5.5. Multi-resolution simulation with complex geometries

Flow simulations between two fixed gears were conducted for demonstrating this method's capability to be used with a complex geometry. The geometry of the simulation is shown in Fig. 21(a). The top gear has 12 teeth, a tip diameter of 42 mm and a tooth depth of 6.75 mm, while the bottom gear has 24 teeth, a tip diameter of 78 mm and a tooth depth of 6.75 mm. The centre distance between the two gears is 55 mm and the minimum gap is 0.68 mm. The pressure

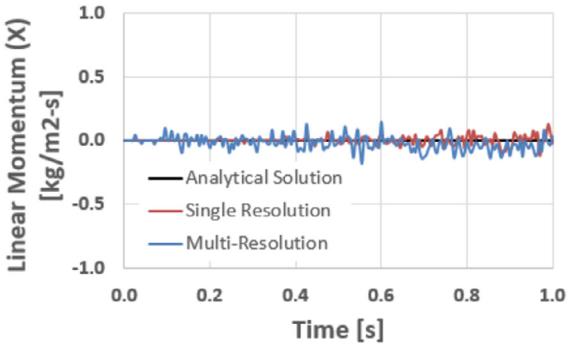

(a) Linear momentum (X direction)

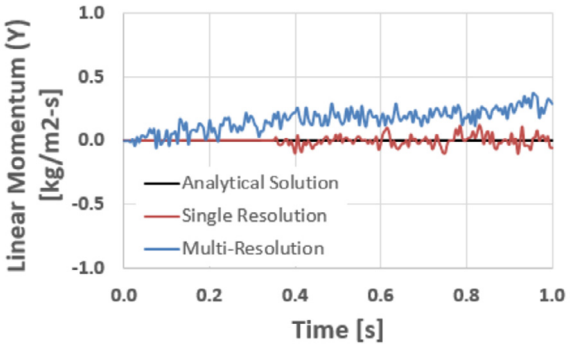

(b) Linear momentum (Y direction)

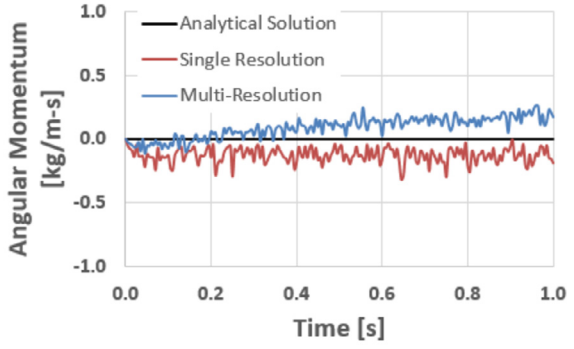

(c) Angular momentum

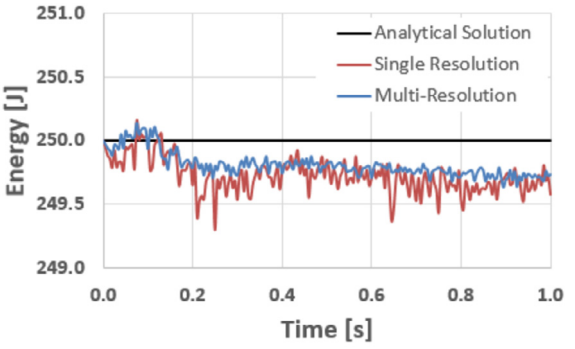

(d) Energy

Fig. 20. Profile of momentum and energy in the Taylor Green vortex simulation.

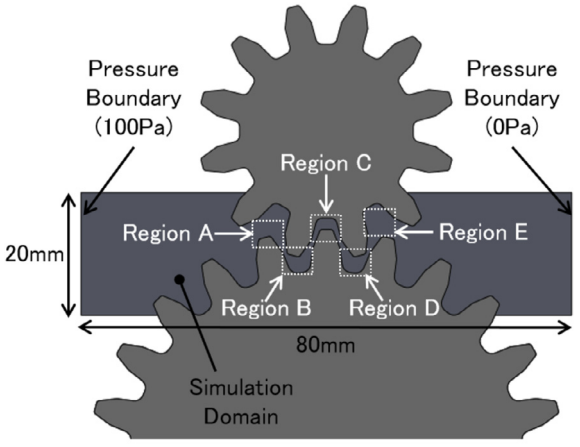

(a) Geometry

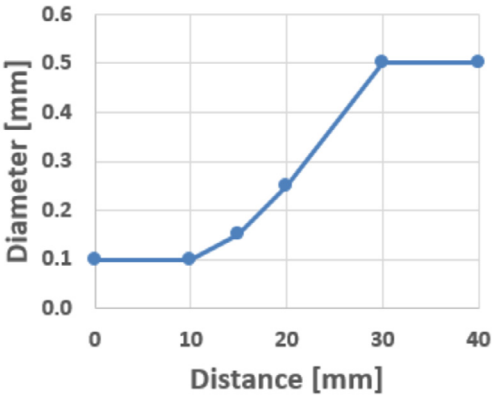

(b) Target Diameter

Fig. 21. Simulation condition of the flow simulation between two gears.

boundary conditions are imposed on both the right and left side of the simulation domain: 100 Pa for the right side and 0 Pa for the left side. The variation of the resolution depends on the distance from the centre of the simulation domain. The function governing the variation on the resolution is shown in Fig. 21(b). The density of the fluid used in the simulation is 1000 kg/m^3 and the dynamic viscosity used is 0.001 Pa s. No external force is considered.

The diameter distribution after simulating up to 0.4 s is shown in Fig. 22. The particles' size becomes smaller as the particles proceed from the inflow region on the left-side boundary towards the narrow region in the middle of the simulation domain and it becomes larger as the particles proceed from the narrow region towards the outflow region located on the right-side boundary. Comparisons of the velocity fields between the Multi-Resolution MPS method and FLUENT in region

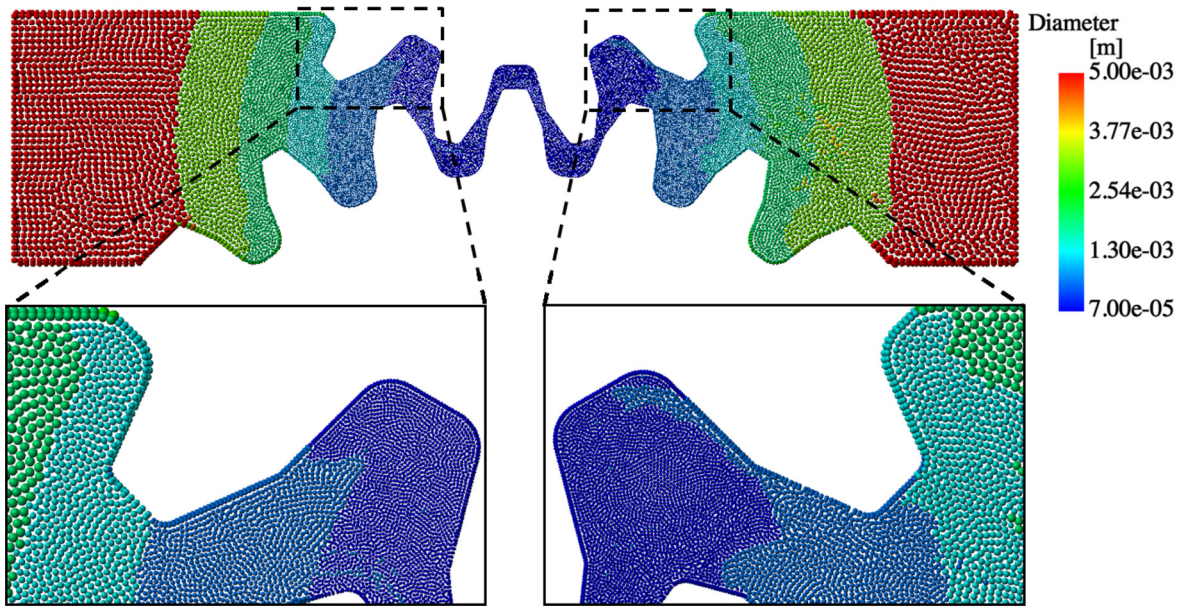

Fig. 22. Diameter distribution between two gears.

A to E, as illustrated in Fig. 21(a), are shown in Fig. 23. Note that the steady flow simulation was conducted by FLUENT, while the unsteady flow simulation until 0.4 s was conducted by the Multi-Resolution MPS method developed in this work. This is because the proposed method is based on a full-Lagrangian method and it is assumed to be applied for unsteady flows. Despite of the difference between the steady and unsteady flows, almost the same flow pattern was obtained with the proposed method when compared with FLUENT. Looking at the detail in Fig. 23, not only the main stream but also the vortices in marginal areas are in good agreement in every region from A to E. This result suggests that this Multi-Resolution MPS method can be successfully applied for simulations with complex geometries.

Since the minimum gap between two gears is 0.68 mm, the particle diameter around the minimum gap should be smaller than 0.1 mm, while the total area of the simulation domain is 1061.6 mm^2. This means that more than 100,000 particles are required if the single resolution simulation is conducted. The average number of the fluid particles in the multi-resolution simulation was only 22,837, which corresponds to the number of particles which is more than 4 times smaller than the number of particles required for the single resolution simulation.

5.6. Multi-resolution dam break simulation with free surface

Dam break simulations with free surfaces are also conducted in this work. Two kinds of dam breaks are considered: the classical dam break simulation without an obstacle and a dam break simulation with a small obstacle.

5.6.1. Dam break simulation without an obstacle

The geometry of the first dam break simulation (without an obstacle) is shown in Fig. 24(a). The width of the vessel is 400 mm and the size of the fluid in the initial state is 100 mm $\times$ 200 mm. The density used is 1000 kg/m^3 while the dynamic viscosity is 0.001 Pa s. The acceleration of gravity f is 9.8 m/s^2. The single resolution simulation was conducted with the diameter of 1 mm and the multi-resolution simulation utilised a diameter range from 1 mm to 5 mm. The target diameter in the multi-resolution simulation depends on the distance from the right-bottom point of the vessel, whose coordinate is (200 mm, 0 mm), as shown in Fig. 24(b). The pressure is monitored at the evaluation point (195 mm, 5 mm) for every 100 time steps.

The fluid motion and the distribution of the particles' diameter for the single and multi-resolution simulations are shown in Fig. 25. In the multi-resolution simulation, particles were split and became smaller during the approach to the right side wall. Even though the smallest target diameter used was 1.0 mm, the smallest diameter obtained in the results was around 0.619 mm. This is because the diameter after particle splitting is defined by Eq. (65) and does not accord with the inputted target diameter completely. After colliding with the right wall, particles move to the left direction and then smaller particles were merged and became larger after entering the low resolution region. Some different sizes of particles were mixed after the particle merging process and this is because there is not always a proper particle available to be merged with. However, the most important point is that the resolution of the specific region, which is the right-bottom edge in this case, is kept higher and this is successfully achieved with this method. The fluid motion of the multi-resolution simulation is similar with that of the single resolution simulation and no instability or unnatural fluid behaviour was observed in the particle splitting and merging processes.

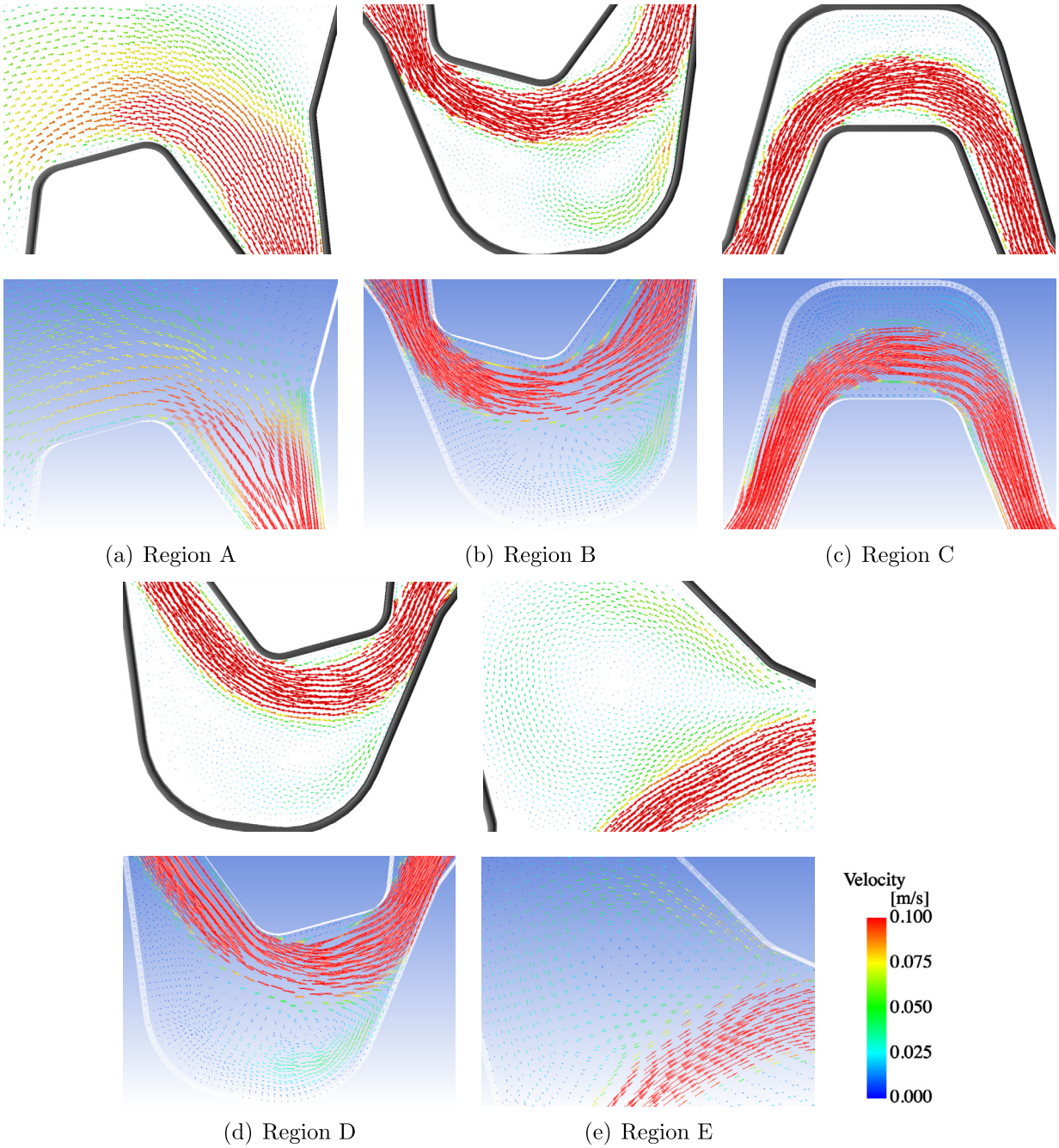

Fig. 23. Comparison of the velocity field between two gears (above: Multi-Resolution MPS method, bottom: FLUENT).

The computational cost for the multi-resolution simulation was considerably smaller than that of the single resolution simulation. The number of fluid particles in the multi-resolution simulation was 1,322 at the time step of 0.15 s, 7,038 at the time step of 0.25 s, 10,557 at the time step of 0.50 s and 9,730 at the time step of 0.75 s. For the single resolution simulation, the number of particles was kept constant with a total of 19,969. The average number of fluid particles throughout the multi-resolution simulation was 7667.3, which means that, when compared with the single resolution simulation, the number of fluid particles was reduced by 61.6% and the computational time was reduced by 61.8%. The fact that the reduction rate of the computational time is roughly the same as that of the number of fluid particles suggests that the computation of the Poisson's equation, which depends on the number of particles, is the most time-consuming part of the calculations. Also, the extra computational time for particle splitting and particle merging for the multi-resolution simulations is proven to be less expensive. This is the major advantage of the Multi-Resolution MPS method.

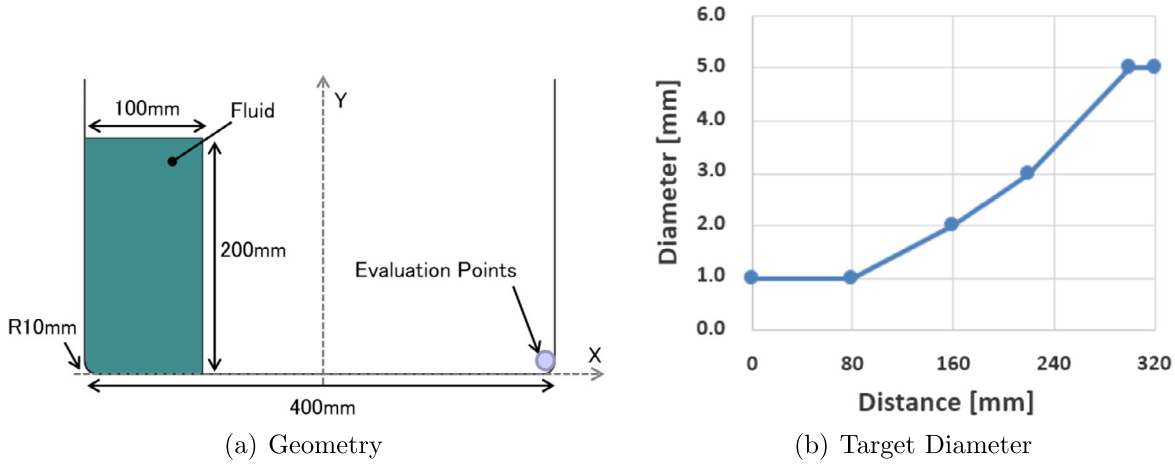

Fig. 24. Simulation condition of the dam break simulation without an obstacle.

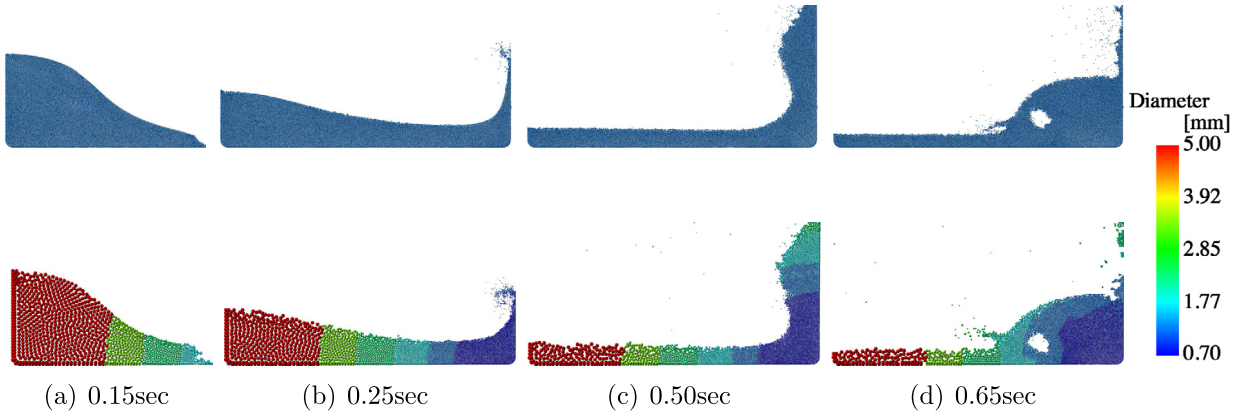

Fig. 25. Comparison of the fluid flow between the single and multi-resolution simulation (above: single resolution, bottom: multi-resolution).

The flow front motions of the single and multi-resolution simulation were compared with experimental results and with the traditional MPS method conducted by Koshizuka and Oka [24]. All the results were plotted in Fig. 26(a) with the non-dimensional fluid width $h^* = h/h_0$ and the non-dimensional time $t^* = t\sqrt{2g/h_0}$, where h is a width of the fluid and $h_0 = 100$ mm is the initial width of the fluid. The results of the three simulations were similar, however, they did not match the experimental results perfectly. However, Koshizuka and Oka [24] showed that the result of the MPS method was in good agreement with that of the Eulerian method and then the simulation results were supposed to be plausible. The fact that the proposed Multi-Resolution MPS method provided a similar behaviour for the flow front when compared with the single resolution method shows that the spatial resolution was able to be changed dynamically without altering the fluid motion accuracy considerably.

The pressure at the evaluation point in Fig. 24(a) was compared between the single and multi-resolution simulations as shown in Fig. 26(b). The profiles of the pressure agreed well while the peek pressure was slightly different with the result of 4433.01 Pa for the single resolution simulation and 4699.80 Pa for the multi-resolution. This is because the pressure value is computed by the Poisson's equation which gathers information from the whole simulation domain including the low resolution region. The multi-resolution simulation cannot provide exactly the same result with the single resolution simulation, yet it is beneficial to obtain approximate results with lower computational costs.

5.6.2. Dam break simulation with a small obstacle

The geometry of the dam break simulation with a small obstacle is shown in Fig. 27(a). The vessel has the width of 400 mm with a small obstacle in the middle of the vessel, located at the bottom of the vessel. The obstacle is as small as 10 mm × 10 mm and therefore particles as small as 1 mm for the diameter are required around the obstacle. The initial size of the fluid is 100 mm × 250 mm. The single resolution simulation with the diameter of 1 mm for the particles and the multi-resolution simulation with the diameter for the particles ranging from 1 mm to 5 mm are conducted. The target diameter in the multi-resolution simulation depends on the distance from the origin point, as shown in Fig. 27(b), so that a finer resolution around the small obstacle can be obtained. The physical values and other simulation conditions are the

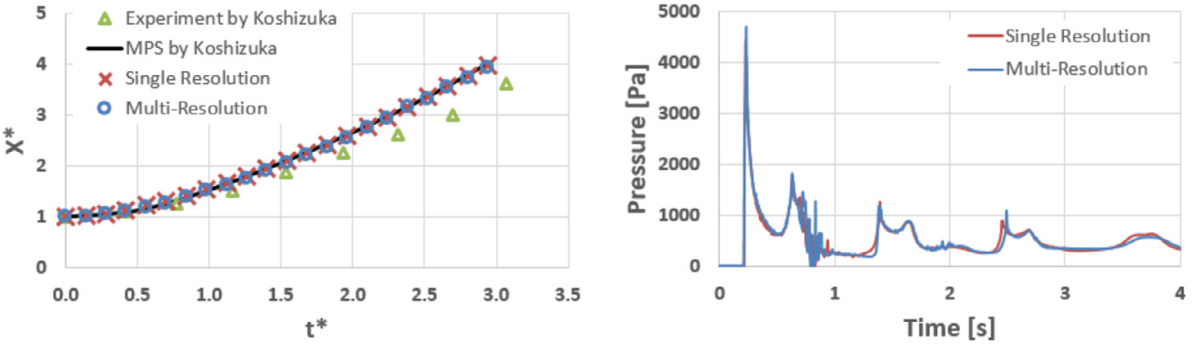

(a) Flow front (b) Pressure

Fig. 26. Simulation results of the dam break simulation without an obstacle.

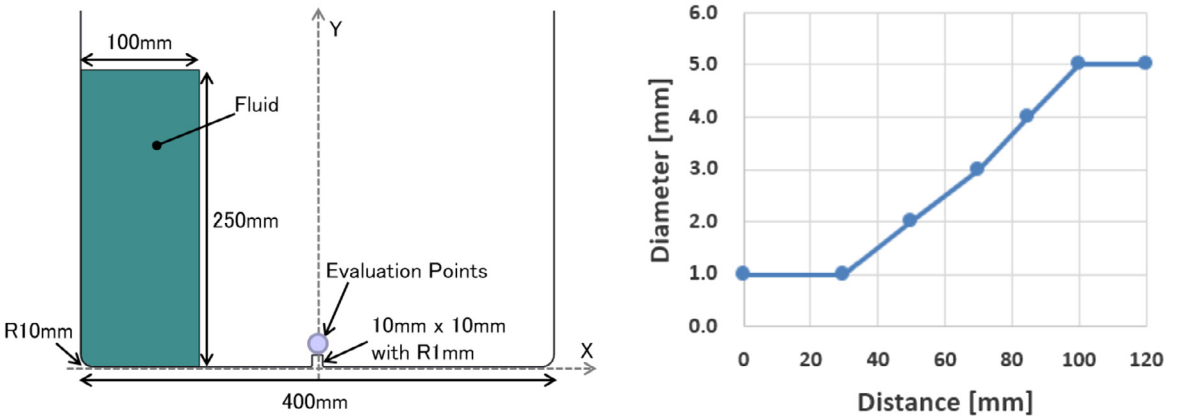

(a) Geometry (b) Target diameter

Fig. 27. Simulation condition of the dam break simulation with an obstacle.

same as for the first dam break example. The pressure and velocity values are monitored at the evaluation point which is 5 mm above the small obstacle.

Comparison of the pressure distribution between the single and multi-resolution simulations before colliding the small obstacle is shown in Fig. 28. The fluid motion and the pressure distribution obtained by the multi-resolution simulation were similar in general to those by the single resolution simulation. Although some differences in the pressure distribution were observed around the small obstacle at 0.11 s, this is due to the way the pressure value are computed as stated above. Such differences in pressure distribution did not influence the fluid motion crucially and then are considered to be acceptable.

The fluid motion and the velocity distribution after the collision with the small obstacle is illustrated in Fig. 29. Both the fluid motion and the velocity field matched well up to 0.65 s, however, the fluid shapes at 1.0 s are different. This is because the characteristic part of the fluid is mainly in the region where the resolution is lower and so the simulation is not accurate anymore. Therefore the pre-selection for the configuration of the resolution should be done carefully.

The number of the fluid particles used in the multi-resolution simulation was 4,291 in average while it was 24,969 throughout the single resolution simulation. In other words, the number of fluid particles was reduced by 82.8% by using the multi-resolution techniques, and as a result, the computational time was reduced by 93.4%. In this case, the main reason why the reduction rate of the computational time is higher than that of the number of the fluid particles is because the size of the time step was able to be larger for the multi-resolution simulation. The particles which had the highest velocity were the splash particles after the fluid collided with the wall and the size of the splash particles in the multi-resolution simulation were larger than that in the single resolution simulation. Then, the time step, which is calculated from Eq. (64), could be larger in the multi-resolution simulation.

The pressure and velocity at the evaluation point in Fig. 27(a) were monitored for every 100 time steps as plotted in Fig. 30. The results for the multi-resolution simulation provided similar pressure and velocity profiles with those of the single resolution simulation until 0.6 s, but there were some differences observed as the simulation went on after that. This is mainly because a particle which had been in a lower resolution region came back to the higher resolution region carrying a bad level of accuracy with it as mentioned above. However, most importantly, the peak velocity at the first fluid

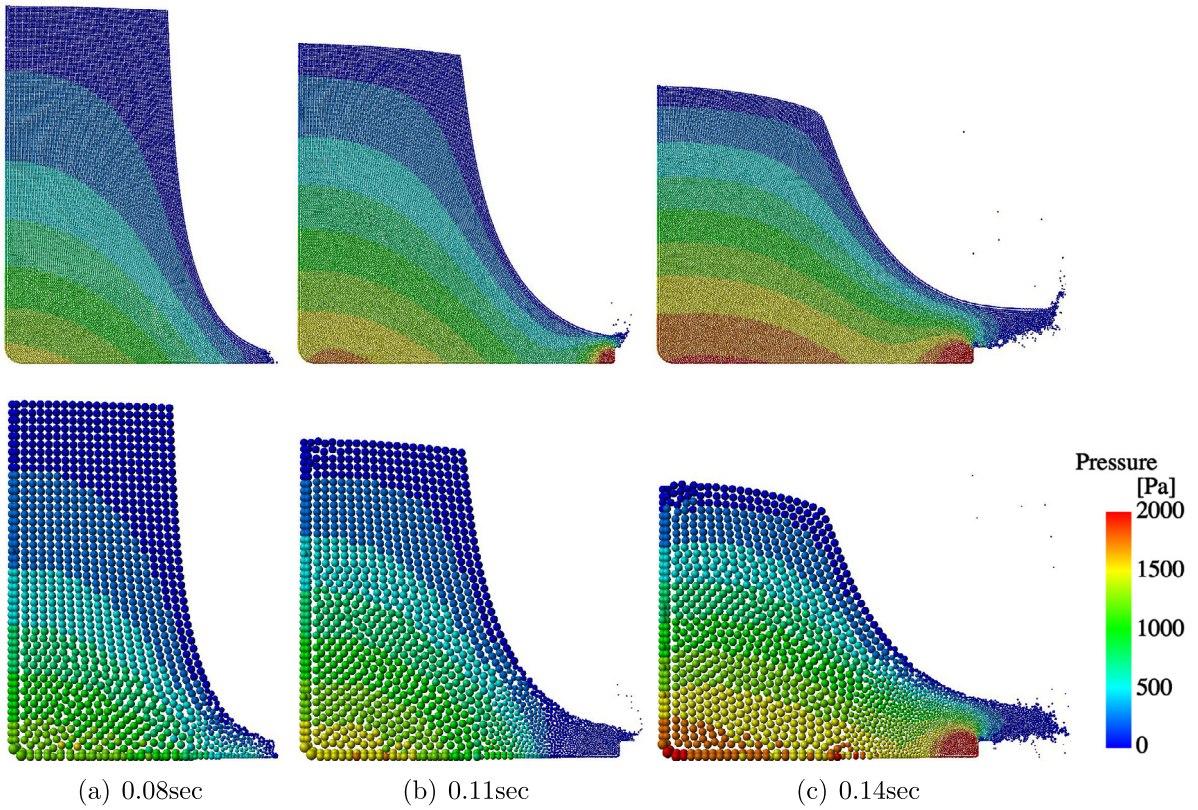

Fig. 28. Comparison of the pressure distribution between the single and multi-resolution simulation (above: single resolution, bottom: multi-resolution).

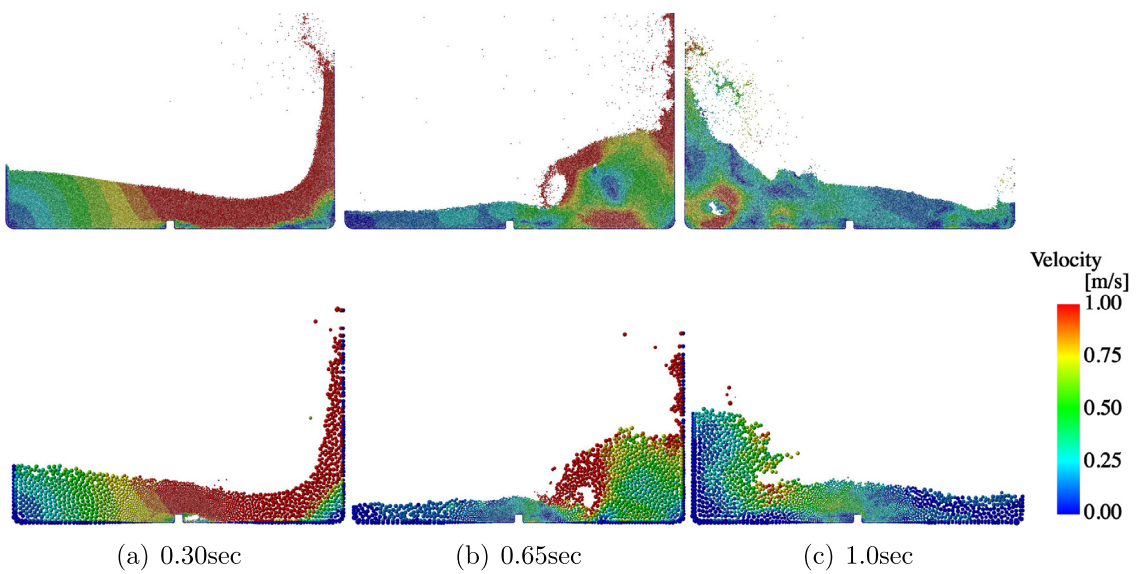

Fig. 29. Velocity distribution of the dam break simulation with an obstacle (above: single resolution, bottom: multi-resolution).

impact around at 0.14 s was almost the same. The multi-resolution technique is beneficial to reduce computational costs, but a proper resolution configuration for a proper problem to be simulated is required. This is a common issue not only for particle methods but also for many other numerical methods.

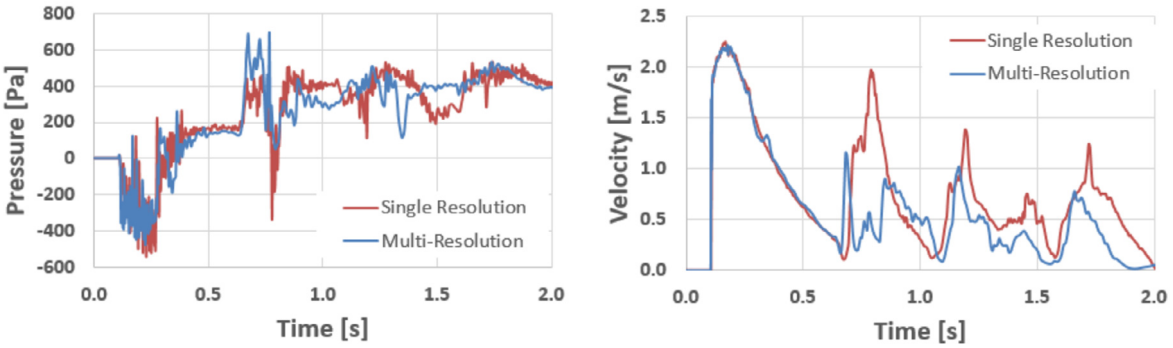

(a) Pressure (b) Velocity

Fig. 30. Pressure and velocity profile in the dam break simulation with an obstacle.

6. Conclusions

The Multi-Resolution MPS method is presented in this paper. The spatial resolution is changed adaptively by the particle splitting and merging algorithms. The LSMPS method is applied to obtain accurate results even if particles have different diameters. The particle shifting algorithm and the surface detection algorithm are modified for a multi-resolution simulation. A new wall boundary scheme, which is represented by polygons, is also improved for a multi-resolution simulation by copying fluid particles around walls and generating imaginary wall particles right on the boundaries. Furthermore, a novel pressure boundary condition, which works arbitrarily for both inflow and outflow boundaries, is proposed. By conducting simulations for channel flows and for free surface flows, the accuracy of the Multi-Resolution MPS method could be verified. Also, it was shown that this method was able to reduce computational costs significantly. Although only two dimensional simulations were conducted in this paper, extension to three dimensions is straightforward.

References

[1] S. Adami, X.Y. Hu, N.A. Adams, A generalized wall boundary condition for smoothed particle hydrodynamics, J. Comput. Phys. 231 (21) (2012) 7057–7075.
[2] B. Adams, M. Pauly, R. Keiser, L.J. Guibas, Adaptively sampled particle fluids, in: Proceedings of ACM SIGGRAPH 2007, ACM Trans. Graph. 26 (3) (2007) 48.
[3] S.J. Cummins, M. Rudman, An SPH projection method, J. Comput. Phys. 152 (2) (1999) 584–607.
[4] G.A. Dilts, Moving-least-squares-particle hydrodynamics I. Consistency and stability, Int. J. Numer. Methods Eng. 44 (8) (1999) 1115–1155.
[5] G.A. Dilts, Moving least-squares particle hydrodynamics II: conservation and boundaries, Int. J. Numer. Methods Eng. 48 (10) (2000) 1503–1524.
[6] A.M. Gambaruto, Computational haemodynamics of small vessels using the Moving Particle Semi-implicit (MPS) method, J. Comput. Phys. 302 (2015) 68–96.
[7] R.A. Gingold, J.J. Monaghan, Smoothed particle hydrodynamics – theory and application to non-spherical stars, Mon. Not. R. Astron. Soc. 181 (1977) 375–389.
[8] J.L. Guermond, P. Minev, J. Shen, An overview of projection methods for incompressible flows, Comput. Methods Appl. Mech. Eng. 195 (44–47) (2006) 6011–6045.
[9] T. Harada, S. Koshizuka, K. Shimazaki, Improvement of wall boundary calculation model for MPS method, Trans. Jpn. Soc. Comput. Eng. Sci. (2008) 20080006 (in Japanese).
[10] S. Heo, S. Koshizuka, Y. Oka, Numerical analysis of boiling on high heat-flux and high subcooling condition using MPS-MAFL, Int. J. Heat Mass Transf. 45 (2002) 2633–2642.
[11] C. Hori, H. Gotoh, H. Ikari, A. Khayyer, GPU-acceleration for Moving Particle Semi-Implicit method, Comput. Fluids 51 (1) (2011) 174–183.
[12] S.M. Hosseini, J.J. Feng, Pressure boundary conditions for computing incompressible flows with SPH, J. Comput. Phys. 230 (19) (2011) 7473–7487.
[13] Y. Huang, C. Zhu, Numerical analysis of tsunami–structure interaction using a modified MPS method, Nat. Hazards 75 (3) (2015) 2847–2862.
[14] H. Ikeda, S. Koshizuka, Y. Oka, Numerical analysis of jet injection behavior for fuel–coolant interaction using particle method, J. Nucl. Sci. Technol. 38 (3) (2001) 174–182.
[15] S. Jeong, J. Nam, S. Hwang, J. Park, M. Kim, Numerical prediction of oil amount leaked from a damaged tank using two-dimensional moving particle simulation method, Ocean Eng. 69 (2013) 70–78.
[16] A. Khayyer, H. Gotoh, A higher order Laplacian model for enhancement and stabilization of pressure calculation by the MPS method, Appl. Ocean Res. 32 (1) (2010) 124–131.
[17] A. Khayyer, H. Gotoh, Enhancement of stability and accuracy of the moving particle semi-implicit method, J. Comput. Phys. 230 (2011) 3093–3118.
[18] A. Khayyer, H. Gotoh, A 3D higher order Laplacian model for enhancement and stabilization of pressure calculation in 3D MPS-based simulations, Appl. Ocean Res. 37 (2012) 120–126.
[19] A. Khayyer, H. Goth, Y. Shimizu, Comparative study on accuracy and conservation properties of two particle regularization schemes and proposal of an optimized particle shifting scheme in ISPH context, J. Comput. Phys. 332 (1) (2017) 236–256.
[20] T. Kikuchi, Y. Michiwaki, T. Kamiya, Y. Toyama, T. Tamai, S. Koshizuka, Human swallowing simulation based on videofluorography images using Hamiltonian MPS method, Comput. Part. Mech. 2 (3) (2015) 247–260.
[21] S. Kitsionas, A.P. Whitworth, Smoothed Particle Hydrodynamics with particle splitting, applied to self-gravitating collapse, Mon. Not. R. Astron. Soc. 330 (2002) 129.
[22] M. Kondo, S. Koshizuka, Improvement of stability in moving particle semi-implicit method, Int. J. Numer. Methods Fluids 65 (6) (2011) 638–654.
[23] S. Koshizuka, H. Tamako, Y. Oka, A particle method for incompressible viscous flow with fluid fragmentation, Comput. Fluid Dyn. J. 4 (1995) 29–46.

[24] S. Koshizuka, Y. Oka, Moving-particle semi-implicit method for fragmentation of incompressible fluid, Nucl. Sci. Eng. 123 (1996) 421–434.
[25] S. Koshizuka, A. Nobe, Y. Oka, Numerical analysis of breaking waves using the moving particle semi-implicit method, Int. J. Numer. Methods Fluids 26 (1998) 751–769.
[26] S. Koshizuka, H.Y. Yoon, D. Yamashita, Y. Oka, Numerical analysis of natural convection in a square cavity using MPS-MAFL, Comput. Fluid Dyn. J. 8 (4) (2000) 485–494.
[27] M. Lastiwka, N. Quinlan, M. Basa, Adaptive particle distribution for smoothed particle hydrodynamics, Int. J. Numer. Methods Fluids 47 (10–11) (2005) 1403–1409.
[28] M. Lastiwka, M. Basa, N.J. Quinlan, Permeable and non-reflecting boundary conditions in SPH, Int. J. Numer. Methods Fluids 61 (7) (2008) 709–724.
[29] B. Lee, J. Park, M. Kim, S. Hwang, Step-by-step improvement of MPS method in simulating violent free-surface motions and impact-loads, Comput. Methods Appl. Mech. Eng. 200 (9–12) (2011) 1113–1125.
[30] A. Leroy, D. Violeau, M. Ferrand, C. Kassiotis, Unified semi-analytical wall boundary conditions applied to 2-D incompressible SPH, J. Comput. Phys. 261 (2014) 106–129.
[31] M.B. Liu, G.R. Liu, K.Y. Lam, Adaptive smoothed particle hydrodynamics for high strain hydrodynamics with material strength, Shock Waves 15 (1) (2006) 21–29.
[32] L.B. Lucy, A numerical approach to the testing of the fission hypothesis, Astron. J. 82 (1977) 1013–1024.
[33] F. Macia, M. Antuono, L.M. Gonzalez, A. Colagrossi, Theoretical analysis of the no-slip boundary condition enforcement in SPH methods, Prog. Theor. Phys. 125 (6) (2011) 1091–1121.
[34] N. Mitsume, S. Yoshimura, K. Murotani, T. Yamada, Explicitly represented polygon wall boundary model for the explicit MPS method, Comput. Part. Mech. 2 (1) (2015) 73–89.
[35] T. Matsunaga, K. Shibata, K. Murotani, S. Koshizuka, Hybrid grid-particle method for fluid mixing simulation, Comput. Part. Mech. 2 (3) (2015) 233–246.
[36] A. Mokos, B.D. Rogers, P.K. Stansby, A multi-phase particle shifting algorithm for SPH simulations of violent hydrodynamics with a large number of particles, J. Hydraul. Res. 55 (2) (2017) 143–162.
[37] J.J. Monaghan, SPH without a tensile instability, J. Comput. Phys. 159 (2) (2000) 290–311.
[38] K. Murotani, I. Masaie, T. Matsunaga, S. Koshizuka, R. Shioya, M. Ogino, T. Fujisawa, Performance improvements of differential operators code for MPS method on GPU, Comput. Part. Mech. 2 (3) (2015) 261–272.
[39] A.P.A. Mustari, Y. Oka, M. Furuya, W. Takeo, R. Chen, 3D simulation of eutectic interaction of Pb–Sn system using Moving Particle Semi-implicit (MPS) method, Ann. Nucl. Energy 81 (2015) 26–33.
[40] P. Nair, G. Tomar, Volume conservation issues in incompressible smoothed particle hydrodynamics, J. Comput. Phys. 297 (15) (2015) 689–699.
[41] K.C. Ng, Y.H. Hwang, T.W.H. Sheu, On the accuracy assessment of Laplacian models in MPS, Comput. Phys. Commun. 185 (10) (2014) 2412–2426.
[42] G. Oger, S. Marrone, D. Le Touze, M. de Leffe, SPH accuracy improvement through the combination of a quasi-Lagrangian shifting transport velocity and consistent ALE formalisms, J. Comput. Phys. 313 (2016) 76–98.
[43] X. Pan, H. Zhang, X. Sun, Numerical simulation of sloshing with large deforming free surface by MPS-LES method, China Ocean Eng. 26 (4) (2012) 653–668.
[44] A. Regmi, H. Shintaku, T. Sasaki, S. Koshizuka, Flow simulation and solidification phenomena of AC_4CH aluminum alloy in semi-solid forging process by explicit MPS method, Comput. Part. Mech. 2 (3) (2015) 223–232.
[45] S. Saso, M. Mouri, M. Tanaka, S. Koshizuka, Numerical analysis of two-dimensional welding process using particle method, Weld. World 60 (1) (2016) 127–136.
[46] K. Shibata, S. Koshizuka, K. Tanizawa, Three-dimensional numerical analysis of shipping water onto a moving ship using a particle method, J. Mar. Sci. Technol. 14 (2) (2009) 214–227.
[47] K. Shibata, S. Koshizuka, T. Tamai, Overlapping particle technique and application to green water on deck, in: International Conference on Violent Flows, 2012, pp. 106–111.
[48] K. Shibata, I. Masaie, M. Kondo, K. Murotani, S. Koshizuka, Improved pressure calculation for the moving particle semi-implicit method, Comput. Part. Mech. 2 (1) (2015) 99–108.
[49] K. Shibata, S. Koshizuka, K. Murotani, M. Sakai, I. Masaie, Boundary conditions for simulating Karman vortices using the MPS method, J. Adv. Simul. Sci. Eng. 2 (2) (2015) 235–254.
[50] Z. Sun, K. Djidjeli, J.T. Xing, F. Cheng, Modified MPS method for the 2D fluid structure interaction problem with free surface, Comput. Fluids 122 (2015) 47–65.
[51] J.W. Swegle, D.L. Hicks, S.W. Attaway, Smoothed particle hydrodynamics stability analysis, J. Comput. Phys. 116 (1) (1995) 123–134.
[52] T. Tamai, S. Koshizuka, Least squares moving particle semi-implicit method, Comput. Part. Mech. 1 (3) (2014) 277–305.
[53] T. Tamai, K. Murotani, S. Koshizuka, On the consistency and convergence of particle-based meshfree discretization schemes for the Laplace operator, Comput. Fluids 142 (2017) 79–85.
[54] M. Tanaka, T. Masunaga, Y. Nakagawa, Multi-resolution MPS method, Trans. Jpn. Soc. Comput. Eng. Sci. (2009) 20090001 (in Japanese).
[55] M. Tanaka, T. Masunaga, Stabilization and smoothing of pressure in MPS method by quasi-compressibility, J. Comput. Phys. 229 (11) (2010) 4279–4290.
[56] Z. Tang, Y. Zhang, D. Wan, Numerical simulation of 3-D free surface flows by overlapping MPS, J. Hydrodynam., Ser. B 28 (2) (2016) 306–312.
[57] Z. Tang, D. Wan, G. Chen, Q. Xiao, Numerical simulation of 3D violent free-surface flows by multi-resolution MPS method, J. Ocean Eng. Mar. Energy 2 (3) (2016) 355–364.
[58] L.J.P. Timmermans, P.D. Miner, F.N. Van De Vosse, An approximate projection scheme for incompressible flow using spectral elements, Int. J. Numer. Methods Fluids 22 (7) (1996) 673–688.
[59] N. Tsuruta, A. Khayyer, H. Gotoh, Space potential particles to enhance the stability of projection-based particle methods, Int. J. Comput. Fluid Dyn. 29 (1) (2015) 100–119.
[60] A. Valizadeh, J.J. Monaghan, A study of solid wall models for weakly compressible SPH, J. Comput. Phys. 300 (1) (2015) 5–19.
[61] R. Xu, P. Stansby, D. Laurence, Accuracy and stability in incompressible SPH (ISPH) based on the projection method and a new approach, J. Comput. Phys. 228 (18) (2009) 6703–6725.
[62] X. Yang, M. Liu, S. Peng, Smoothed particle hydrodynamics modeling of viscous liquid drop without tensile instability, Comput. Fluids 92 (20) (2014) 199–208.
[63] H.Y. Yoon, S. Koshizuka, Y. Oka, A particle-gridless hybrid method for incompressible flows, Int. J. Numer. Methods Fluids 30 (1999) 407–424.
[64] T.G. Zhang, S. Koshizuka, K. Kazuya, K. Murotani, E. Ishii, Improved wall weight function with polygon boundary in moving particle semi-implicit method, Trans. Jpn. Soc. Comput. Eng. Sci. (2015) 20150012.
[65] X. Zhu, L. Cheng, L. Lu, B. Teng, Implementation of the moving particle semi-implicit method on GPU, Sci. China, Phys. Mech. Astron. 54 (3) (2011) 523–532.